Stockholms
universitet

Conformations of Flexible Oligosaccharides: Molecular Simulations and NMR Spectroscopy

Robert Pendrill

© Robert Pendrill, Stockholm 2013
Cover picture: *Spectral densities.*

ISBN 978-91-7447-808-2

Printed in Sweden by US-AB, Stockholm 2013
Distributor: Department of Organic Chemistry, Stockholm University

The model is a hypothetical conjecture
that might or might not summarize and/or
explain important features of the data.
[Unknown]

Abstract

The conformational preferences of several oligosaccharides are investigated herein using a combination of NMR spectroscopy and molecular dynamics (MD) simulations, focusing on the torsion angles associated with the glycosidic linkages.

Strategies for obtaining usable J-HMBC spectra for carbons with an adjacent ^{13}C label are described. By employing a selective pulse or a constant time modification, spectra free from interferences are obtained for site-specifically ^{13}C labeled oligosaccharides.

Intermolecular hydrogen bonding in sucrose is investigated using MD simulations performed at different concentrations. One of the most frequent intermolecular hydrogen bonds in the simulations, $\mathrm{O3}f\cdots\mathrm{HO3}g$, was detected using the HSQC-TOCSY NMR experiment.

Based on MD simulations and NMR spectroscopy, the conformational ensemble for a trisaccharide segment of the Le^{a}Le^{x} hexasaccharide is proposed to feature conformational exchange between conformations with positive and negative values for the ψ_3 torsion angle in the β-D-Glc*p*NAc-(1→3)-β-D-Gal*p* linkage.

Using MD simulations, the conformation of the *N*-acetyl group is shown to influence the glycosidic conformation at a nearby linkage in two oligosaccharides.

Short (1→6)-linked oligosaccharides are shown to exhibit conformational exchange at the ω and ψ torsion angles. Notably, the former torsion angle populates states with $\psi \approx \pm 90^\circ$. Conformationally sensitive homo- and heteronuclear coupling constants are determined using various NMR experiments. The experimental data, including effective distances from NOESY obtained for two of the compounds, is used to improve the representation of the ω torsion angle in the CHARMM36 force field.

List of Publications

This thesis is based on the following papers, which are referred to in the text by their Roman numerals.

I Suppressing One-Bond Homonuclear ^{13}C,^{13}C Scalar Couplings in the J-HMBC NMR Experiment: Application to ^{13}C Site-Specifically Labeled Oligosaccharides.
Pendrill, R.; Sørensen, O. W.; Widmalm, G.
Submitted for publication

II Direct Evidence for Hydrogen Bonding in Glycans: A Combined NMR and Molecular Dynamics Study.
Battistel, M. D.; Pendrill, R.; Widmalm, G.; Freedberg, D. I.
J. Phys. Chem. B **2013**, *117*, 4860–4869.
Supporting information available online

III Conformational Dynamics of a Central Trisaccharide Fragment of the Le^{a}Le^{x} Tumor Associated Antigen Studied by NMR Spectroscopy and Molecular Dynamics Simulations.
Zaccheus, M.; Pendrill, R.; Jackson, T. A.; Wang, A.; Auzanneau, F.-I.; Widmalm, G.
European J. Org. Chem. **2012**, 4705–4715.

IV Glycan Synthesis, Structure, and Dynamics: A Selection.
Pendrill, R.; Jonsson, K. H. M.; Widmalm, G.
Pure Appl. Chem. **2013**, *85*, 1759–1770.

V Conformation and Dynamics at a Flexible Glycosidic Linkage Revealed by NMR Spectroscopy and Molecular Dynamics Simulations: Analysis of β-L-Fuc$p$-(1→6)-α-D-Glc$p$-OMe in Water Solution.
Pendrill, R.; Säwén, E; Widmalm, G.
J. Phys. Chem. B. In press, DOI: 10.1021/jp409985h

VI Conformational Properties of α/β-(1→6)-linked Oligosaccharides: Hamilton Replica Exchange MD Simulations and NMR experiments.
Patel, D. S.†; Pendrill, R.†; Mallajosyula, S. S.; Widmalm, G.; MacKerell, Jr., A. D.
Manuscript in preparation

†Authors contributed equally to this work.
Reprints of the papers were made with permission from the publishers.

Related publications not included in this thesis

Complete ^{1}H and ^{13}C NMR Chemical Shift Assignments of Mono- to Tetrasaccharides as Basis for NMR Chemical Shift Predictions of Oligosaccharides Using the Computer Program CASPER.
Rönnols, J.; Pendrill, R.; Fontana, C.; Hamark, C.; d'Ortoli, T. A.; Engström, O.; Ståhle, J.; Zaccheus, M. V.; Säwén, E.; Hahn, L. E.; Iqbal, S.; Widmalm, G.
Carbohydr. Res. **2013**, *380*, 156–166.

Solid-State NMR Characterization of the Molecular Conformation in Disordered Methyl α-L-Rhamnofuranoside.
Harper, J. K.; Tishler, D.; Richardson, D.; Lokvam, J.; Pendrill, R.; Widmalm, G.
J. Phys. Chem. A **2013**, *117*, 5534–5541.

Stochastic Modeling of Flexible Biomolecules Applied to NMR Relaxation. 2. Interpretation of Complex Dynamics in Linear Oligosaccharides.
Kotsyubynskyy, D.; Zerbetto, M.; Soltesova, M.; Engström, O.; Pendrill, R.; Kowalewski, J.; Widmalm, G.; Polimeno, A.
J. Phys. Chem. B **2012**, *116*, 14541–14555.

Glycan Structure of a High-Mannose Glycoprotein from Raman Optical Activity.
Johannessen, C.; Pendrill, R.; Widmalm, G.; Hecht, L.; Barron, L. D.
Angew. Chem., Int. Ed. **2011**, *50*, 5349–5351.

NMR Analysis of Conformationally Dependent $^nJ_{\mathrm{C,H}}$ and $^nJ_{\mathrm{C,C}}$ in the Trisaccharide α-L-Rha$p$-(1→2)[α-L-Rha$p$-(1→3)]-α-L-Rha$p$-OMe and a Site-Specifically Labeled Isotopologue thereof.
Jonsson, K. H. M.; Pendrill, R.; Widmalm, G.
Magn. Reson. Chem. **2011**, *49*, 117–124.

Contents

Abstract **v**

List of Publications **vii**

Abbreviations **xi**

1 Introduction **1**

1.1 Carbohydrates 2
1.2 NMR spectroscopy 5
1.3 MD simulations 9
1.4 Conformational analysis of carbohydrates 9
1.5 Aims 11

2 J-HMBC: Suppressing Interference from ^{13}C Labeling (Paper I) **13**

2.1 Background 13
2.2 Pulse programs 14
2.3 Experimental evaluation 15
2.4 Conclusions 18

3 Hydrogen Bonding in Sucrose: Experimental Evidence and MD Simulations (Paper II) **19**

3.1 Background 19
3.2 Molecular modeling 21
3.3 Conclusions 27

4 Conformation of a Central Trisaccharide in Le^{a}Le^{x} (Paper III) **29**

4.1 Background 29
4.2 MD simulations 30
4.3 Comparison with NMR spectroscopy 32
4.4 Conclusions 35

5 Involvement of the *N*-Acetyl Group in Glycosidic Conformation (Papers III and IV) 37
5.1 Background 37
5.2 The Le^{a}Le^{x} trisaccharide 38
5.3 The *N*-acetyl group in LNF-1 41
5.4 Conclusions 43

6 Conformation and Dynamics of β-L-Fuc*p*-(1→6)-α-D-Glc*p*-OMe (Paper V) 45
6.1 Background 45
6.2 Conformation 46
6.3 Interactions with water from MD 49
6.4 Dynamics 50
6.5 Conclusions 54

7 Conformations of (1→6)-Linked Di- and Trisaccharides (Paper VI) 57
7.1 Background 57
7.2 NMR spectroscopy 57
7.3 Force field verification 60
7.4 Conclusions 67

8 Conclusion and Outlook 69

Acknowledgments 71

Bibliography 73

Abbreviations

gg	*gauche–gauche* (O5,O6 and C4,O6)
gt	*gauche–trans*
tg	*trans–gauche*
f	Furanose – if preceded by a residue abbreviation
p	Pyranose
CT	Constant time
Fru	Fructose
Fuc	Fucose
Gal	Galactose
Glc	Glucose
HECADE	Heteronuclear couplings from ASSCI-domain experiments with E.COSY-type cross peaks
HMBC	Heteronuclear multiple-bond correlation
HMQC	Heteronuclear multiple-quantum coherence
HSEA	Hard-sphere *exo*-anomeric effect
HSQC	Heteronuclear single-quantum coherence
ISPA	Isolated spin-pair approximation
J-HMBC	J-resolved HMBC
LPS	Lipopolysaccharide
Man	Mannose
MD	Molecular dynamics
Neu	Neuraminic acid
NOE(SY)	Nuclear Overhauser effect (spectroscopy)
PDF	Probability distribution function
PMF	Potential of mean force
RDC	Residual dipolar coupling
ROE(SY)	Rotating frame Overhauser effect (spectroscopy)
STEP	Selective TOCSY-edited preparation
T-ROE(SY)	Transverse rotating frame Overhauser effect (spectroscopy)

1. Introduction

The wide range of molecules in the class of carbohydrates fulfill a vast range of functions in all living organisms, including structural roles and energy storage. Carbohydrates are also involved in signaling and recognition inside and between living cells. In fact, all cells in nature are densely covered by carbohydrates, and many lipids and proteins bear attached carbohydrates.[1] An example of how subtle differences in carbohydrate structure can lead to dramatic effects is found in the human ABO blood group system. The substitution of the *N*-acetyl group in the A antigen by an hydroxyl group in the B antigen (Figure 1.1) is sufficient to provoke a lethal response in a mismatched blood transfusion.

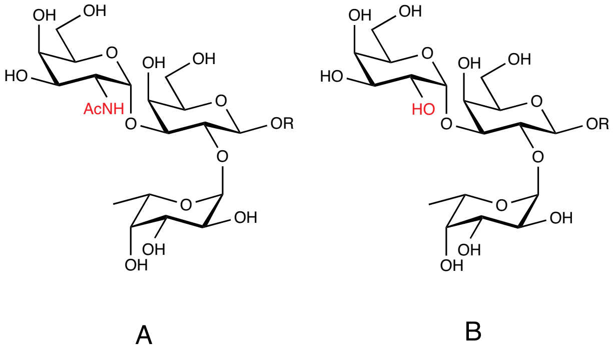

Figure 1.1: The human A and B blood group determinants.

The unraveling of relationships between molecular structure and biological function as well as other properties requires knowledge of the conformations, or shapes, of molecules.[2] For many molecules there is no straightforward way of determining the conformation directly from the way the atoms are connected. The task of defining the conformations of molecules must therefore be guided by experimental observations. As we extend the knowledge on conformations of molecules, the understanding of factors determining the conformational preferences is advanced and consequently our ability to predict conformations is improved.

1.1 Carbohydrates

1.1.1 Constitution of carbohydrates

The smallest carbohydrates are monosaccharides of which glucose is a well-known example. Common to all sugar residues is having a few carbons and a high density of hydroxyl (alcohol) groups. Differences arise from variations in length of the carbon chain, stereochemistry, and other chemical modifications.

Oligo- and polysaccharides consist of monosaccharides joined together at the anomeric carbon and one of the hydroxyl groups. Typically, the residues are found in the form of five- or six-membered rings denoted furanoses and pyranoses respectively. At the anomeric carbon, the linkage can be formed in two different orientations referred to as α and β depending on the stereochemistry; for most pyranoses the α stereochemistry corresponds to an axial orientation for the anomeric substituent.

From the pyranose ring forms alone, two glucose residues can be joined together by a glycosidic bond in 11 different ways. The possibility of several linkage sites allows the formation of branched structures. This way of forming oligo- and polymers is unique among the biopolymers. In contrast, polynucleotides and polypeptides are joined together linearly at two specific ends of the monomeric unit, viz. the amine functionality and the carboxylic acid of an amino acid in the case of a polypeptide.

Three examples of biologically occurring oligosaccharides are shown in Figure 1.2, demonstrating the diversity attained by variation of constituent monosaccharides and linkage types.

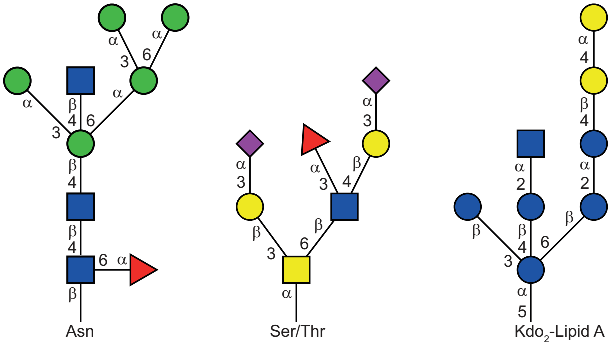

Figure 1.2: Examples of biologically occurring oligosaccharides; a bisected N-glycan (*left*), a core 2 O-glycan (*center*), and the short-chain LPS from *Moraxella catarrhalis* serotype A (*right*).[1,3] Legend: 🟢 Man, 🔵 Glc, 🟦 GlcNAc, 🟡 Gal, 🟨 GalNAc, ◆ NeuAc, and 🔺 Fuc.

1.1.2 Conformations of carbohydrates

The overall conformational preferences of carbohydrates can be divided into two parts; the ring conformation and the linkage conformation. Additional degrees of freedom such as exocyclic groups affect the local shape of the molecule. In the case of much larger structures than those studied herein, e.g. polysaccharides, large-scale conformational effects must be considered.[4,5] For the majority of the pyranose monomers, the preferred ring conformation is the one of the two chair forms having the most substituents in equatorial positions, since this minimizes strain. The exception is at the anomeric position, where an electronegative substituent prefers the axial orientation, an observation termed the anomeric effect.[6] For D and L sugars these considerations lead to the preferred pyranose ring conformations typically being the $^4C_1$ and $^1C_4$ chair conformations, respectively. The $^4C_1$ conformation corresponds to the form shown in Figure 1.3, i.e. with carbon 4 above the plane of the chair and carbon 1 below. While the pyranose monosaccharide residues appearing in this thesis are not completely rigid,[7] alternative ring conformations are not expected to contribute significantly to the overall shapes. The overall conformation can thus be described adequately by defining the orientation around the bonds connecting the residues (Figure 1.3).

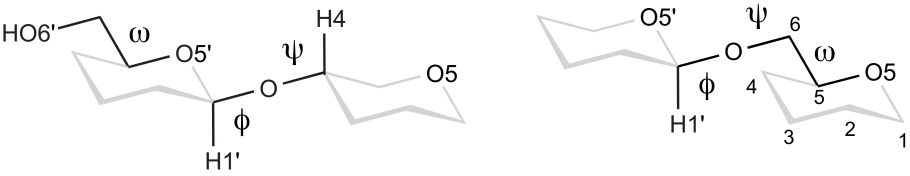

Figure 1.3: Principal degrees of freedom and the numbering convention shown for schematic disaccharides joined by a β-(1→4)-linkage (*left*) or a (1→6)-linkage (*right*).

The glycosidic linkage orientations are expressed in torsion angles defined by atoms in sets of four; throughout this thesis, the convention shown in Figure 1.3 is used for (1→n)-linkages unless otherwise specified;[i]

$$\phi \quad : \quad \text{H1'–C1'–O}n\text{–C}n \tag{1.1}$$

$$\psi \quad : \quad \text{C1'–O}n\text{–C}n\text{–H}n \tag{1.2}$$

$$\omega \quad : \quad \text{O6–C6–C5–O5} \tag{1.3}$$

---

[i] Note that this convention differs from that preferred by IUPAC[8] and which is used in Papers II and VI.

For (1→6)-linked carbohydrates, ψ is usually defined using C5 rather than Hn since there are two hydrogens at C6. In addition the ω torsion angle contributes to the overall conformation in this case, whereas for the other linkage possibilities only ϕ and ψ determine the orientation of the individual rings with respect to each other.

Influences on conformation

Certain orientations are known to be preferred with respect to the aforementioned torsion angles. Generally, repulsive steric interactions maximize the distance between non-bonded atoms. Locally, this means that staggered conformations are favored over eclipsed conformations.

Conformational preferences are also influenced by stereoelectronic factors. The *exo*-anomeric effect governs the ϕ torsion and favors orientations where overlap between exocyclic oxygen lone pairs and the O5'-C1' antibonding orbital is maximized,[9] as depicted in Figure 1.4. For the ω torsion, conformations having the two oxygens in a *gauche* relationship are favored,[10,11] while one of the conformations is disfavored by repulsive interactions with the substituent at the 4th position (Figure 1.5).[12]

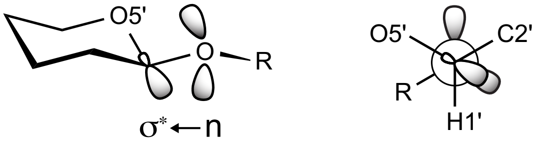

Figure 1.4: Rationalization for the *exo*-anomeric effect based on overlap between a glycosidic oxygen lone pair and the O5'-C1' antibonding orbital.

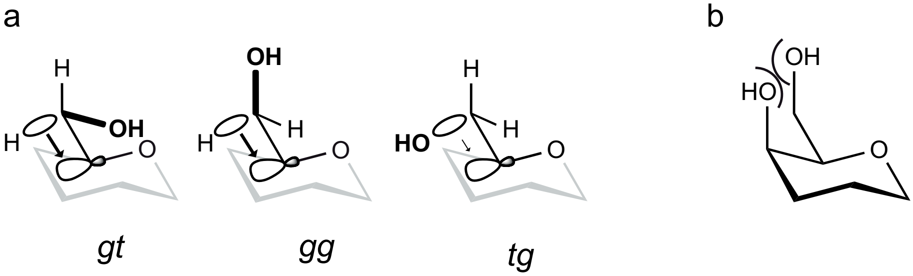

Figure 1.5: Factors affecting the stability of the three rotamers of the ω torsion angle. (a) Hyperconjugation which favors overlap of bonding CH orbitals with antibonding CO orbitals, and (b) steric interactions, disfavoring orientations in which O6 and O4 adopt a pseudo-1,3-diaxial arrangement.

Depending on the linkage type and residue identity, intramolecular hydrogen bonding across the glycosidic linkage can occur. Hydrogen bonding from one residue to the O5' atom in the next residue is frequently found in crystal structures of carbohydrates,[13] as shown for β-cellobiose in Figure 1.6. Such hydrogen bonding is frequently found in gas-phase calculations. In aqueous solution, hydrogen bonding with water reduces the occurrence and importance of intramolecular hydrogen bonding.[14–16] However, the O5'$\cdots$HO3 hydrogen bond depicted in Figure 1.6 was recently shown to exist for cellobiose in aqueous solution using neutron diffraction.[17] While trans-glycosidic hydrogen bonding is typically present in aqueous MD simulations of disaccharides,[18] this may well be a consequence of the particular conformations adopted rather than actually stabilizing these conformations.[19]

In addition to the disruption of intramolecular hydrogen bonding, water and carbohydrates make specific interactions in aqueous solution,[21] which likely influence both the conformation and function of carbohydrates.[22,23]

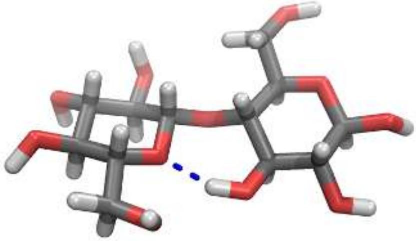

Figure 1.6: Molecular model of β-cellobiose generated from coordinates obtained by X-ray crystallography,[20] with the O5'$\cdots$HO3 hydrogen bond indicated by blue dashes.

1.2 NMR spectroscopy

The prevailing spectroscopic technique in structural and conformational studies of carbohydrates is nuclear magnetic resonance (NMR) spectroscopy.[24,25] In the presence of a magnetic field, nuclei with nonzero spin become sensitive to manipulation by electromagnetic radiation. The different quantized spin states have different energies, leading to a slight population difference at equilibrium, as well as a resonance frequency corresponding to the energy difference. Fortunately, nuclei of the same kind usually have slightly different resonance frequencies due to differences in their chemical environments, making it possible to assign frequencies to individual nuclei within a molecule. The difference in frequency compared to a certain reference compound is termed the chemical shift. For the work described in this thesis, ^{1}H and ^{13}C nuclei have been used, of which ^{1}H is the most sensitive one, due to a large gyromagnetic ratio as well as a close to 100% natural abundance.

Through various NMR experiments, interactions between nuclei as well as motional properties can be probed. One particularly appealing aspect is the possibility of conducting experiments in solutions at close to physiological conditions, e.g. in water at body temperature.

1.2.1 NMR parameters related to conformation

The most direct NMR parameter, the chemical shift, contains information on conformational preferences.[11,26–28] For example, an equation relating ^{13}C glycosylation shifts and the value of the ψ torsion angle was published by Bock et al.[29] However, the use of chemical shifts in conformational analysis of carbohydrates has largely been used in a qualitative sense, e.g. in a recent example where chemical shift arguments were used to support the notion of a non-classical $CH\cdots O$ hydrogen bond in the Le^{x} antigen.[30] With improved quantum mechanical calculations, it is possible that useful relationships between chemical shifts and glycosidic conformation can be derived.[31,32]

While there are many other NMR parameters, such as RDCs,[33] in use for the determination of carbohydrate conformation, the two which have found most use are scalar couplings and NOEs; these are also the ones used in the work described herein.

For molecules undergoing conformational exchange on a short time scale compared to the frequency difference of the individual conformations, NMR parameters such as chemical shifts and scalar couplings will be population-weighted averages.[34]

Scalar coupling

Two spins are said to be coupled if the resonance frequency of one nucleus is affected by the spin state of the other. For scalar couplings, this interaction is mediated by electrons and typically limited to atoms no further than three or four bonds away from each other. The magnitude of the interaction, the scalar coupling constant, is often related to a torsion angle and is thus of high interest for conformational studies.[35] The relationship can be expressed as a Karplus-type equation:

$$J(\theta) = A\cos^2\theta + B\cos\theta + C \tag{1.4}$$

where J is the coupling constant, θ is the torsion angle, and A, B and C are constants. The constants depend on the system under study and in some cases additional terms are used.

Relationships have been devised for the conformational analysis of carbohydrates, with different equations for the ϕ and ψ torsion angles of the glycosidic bond and for the ω torsion angle, as shown in Figure 1.7.[36–38]

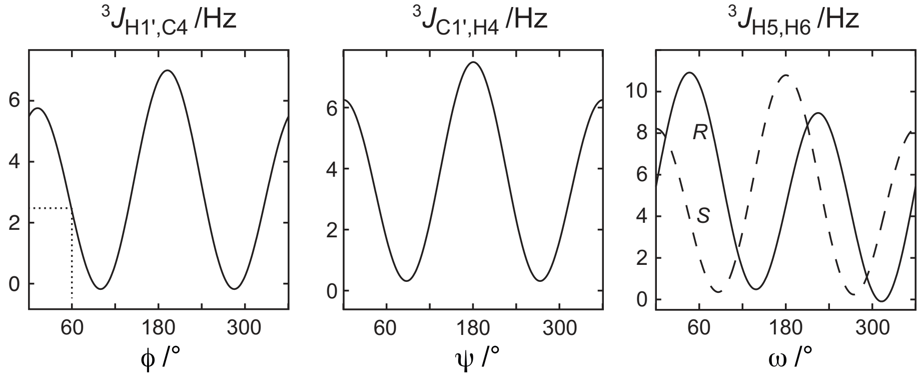

Figure 1.7: Karplus-type relations for the torsion angles ϕ, ψ, and ω. The dotted line at 2.3 Hz in the plot for the ϕ coupling constant corresponds to the value in an idealized *exo*-anomeric conformation, e.g. with $\phi = +60°$ for a β-D-linkage.

When both of the nuclei involved in the coupling have a high abundance, the value can often be extracted from the splitting in a one-dimensional spectrum, either directly or via total line-shape analysis.[39] This is typically the case for $^nJ_{\mathrm{HH}}$ coupling constants, or when the molecule has been isotopically labeled. Several methods have been developed for the measurement of long-range coupling constants between protons and low-abundance nuclei.[40,41] In the included work the J-HMBC[42] and HSQC-HECADE[43] experiments have been used for the determination of heteronuclear $^nJ_{\mathrm{CH}}$ coupling constants at natural ^{13}C abundance.

Nuclear spin relaxation

Any perturbation to the equilibrium magnetization in an ensemble of nuclear spins will increase the energy of the system. The process of releasing this excess energy, nuclear spin relaxation, is intimately linked to both motion and conformation. A division can be made between longitudinal (T_1) and transverse (T_2) relaxation. The former is the return to the equilibrium populations of spin states while the latter is the loss of coherence, or transverse magnetization. The names T_1 and T_2 refer to the time constants for the exponential decays of the two kinds of perturbations.

For an oligosaccharide without any isotopic labeling, ^{13}C relaxation is typically dominated by dipole-dipole interactions with directly bound ^{1}H nuclei. By assuming a CH bond length (r_{CH}) equal to 1.117 Å,[44] the motional contribution to observed ^{13}C relaxation times can be singled out, giving the following relationship between motion and the T_1 relaxation time:[45]

$$T_{1(\mathrm{DD})}^{-1} = \frac{d_{\mathrm{CH}}^2}{4}\left[J(\omega_{\mathrm{H}} - \omega_{\mathrm{C}}) + 3J(\omega_{\mathrm{C}}) + 6J(\omega_{\mathrm{H}} + \omega_{\mathrm{C}})\right] \tag{1.5}$$

in which $d_{\mathrm{CH}} = -\frac{\mu_0}{4\pi}\hbar\gamma_{\mathrm{C}}\gamma_{\mathrm{H}}r_{\mathrm{CH}}^{-3}$, μ_0 is the permittivity of vacuum, $\hbar$ is the reduced Planck constant, and γ is the gyromagnetic ratio of ^{1}H and ^{13}C as indicated by the subscripts. $J(\omega)$ is the reduced spectral density at the angular frequency ω, which for a rigid molecule undergoing isotropic reorientation with a correlation time τ_{c} is

$$J(\omega) = \frac{2}{5}\left(\frac{\tau_{\mathrm{c}}}{1 + \omega^2\tau_{\mathrm{c}}^2}\right) \tag{1.6}$$

A common approach to the interpretation of relaxation rates in terms of molecular motion is through the model-free approach which uses more complex spectral density functions.[46]

The Nuclear Overhauser effect

For proton relaxation, there are typically many surrounding protons contributing to the observed T_1 and T_2 relaxation times. By capitalizing on the NOE, experiments such as NOESY[47] and T-ROESY[48] give access to the dipole-dipole cross-relaxation rates for individual proton-proton interactions. Under certain assumptions, referred to as the isolated spin-pair approximation (ISPA), cross-relaxation rates are proportional to the inverse 6th power of the distance,[49] making them highly valuable in conformational studies.[50] The proportionality constant can be calculated if the cross-relaxation rate, σ_{ref}, is measured for an interaction with a known distance, r_{ref}, allowing the cross-relaxation rate, σ_{ij}, between i and j to be translated into a distance, r_{ij}, according to equation 1.7.

$$r_{ij} = r_{\mathrm{ref}}\left(\frac{\sigma_{\mathrm{ref}}}{\sigma_{ij}}\right)^{1/6} \tag{1.7}$$

If cross-relaxation rates are measured by both NOESY and T-ROESY experiments, the correlation time can be determined from the ratio of the two rates.[51]

1.3 MD simulations

The time evolution of a molecular system is simulated in molecular dynamics (MD) simulations based on energies calculated within a force field. To the extent that the force field and simulation protocol reproduce the experimental system, detailed insight can be gained into events occurring at an atomistic level and in the time scale of picoseconds to microseconds. Thus, phenomena that are not accessible by experimental methods can be studied.[52]

The force field consists of a set of equations and parameters which together describe the internal energy for a given configuration of atoms. Typically these are parametrized with a particular class of molecules in mind and are not expected to perform particularly well for other classes of molecules. A plethora of force fields for carbohydrates has been developed in the quest for increasing accuracy.[53] Carbohydrate force fields appearing in this thesis are the PARM22/SU01 force field,[54] the CHARMM all-atom additive force field[55,56] and the GLYCAM06 force field.[57]

Given enough time, a representative ensemble of states can be collected and from these values of observable parameters can be calculated and compared with experimental values in order to validate the simulation. In order for the ensemble over time to be representative of an equilibrium ensemble, the simulation must be performed for a time period much longer than the time scales of all relevant processes. In the case of carbohydrates, this means that simulations typically need to be extended for at least a few 100 ns in order to reach convergence.[58]

Given the importance of water for the behavior of carbohydrates,[15] MD simulations are preferably performed with explicit water rather than treating solvation implicitly. For a dilute solution of a carbohydrate this means that the larger part of the computation time is spent on the simulation of water.

1.4 Conformational analysis of carbohydrates

The determination of a conformational distribution from experimental parameters determined by NMR spectroscopy is far from trivial. Generally, there are not many experimental parameters reporting on glycosidic conformation; unless RDCs are measured, typically two long-range heteronuclear coupling constants and a small number of trans-glycosidic NOEs are available.

If it is known that only one conformation contributes to the observed data, it is possible to map the regions of conformational space that are compatible with experiment. However, the conformation derived from such a procedure is meaningless if conformational averaging is occurring.[59] Even if a single conformation can explain experimental parameters, the possibility of conformational averaging cannot be ruled out. However, the inability to rationalize experimental observations with a single conformation is a good indication that conformational averaging is occurring.

There is no good reason to assume that every one, or any, of the conformations contributing to the observed values agrees with experiment. Rather, it is the ensemble of the contributing conformations that should agree with the experimental parameters. There can be an infinite number of possible conformational ensembles that agree with experiment, since the contributing conformations and their respective populations are unknown. This is particularly troubling for the case of oligosaccharides considering the limited amount of experimental parameters typically available.

Several approaches have been proposed in order to derive the most likely conformational ensemble from experimental observation alone, e.g. the maximum entropy,[60] CUPID,[61] and similar[62] methods. However, these generally require an amount of experimental parameters that is larger than what is typically available for an oligosaccharide; otherwise an unreasonable conformational distribution can be obtained.[63]

Due to the difficulties in deriving a conformational ensemble from only experimental parameters, it is more appropriate to use experimental parameters as a verification of a conformational ensemble derived from molecular modeling methods,[64] e.g. MD simulations.

A measure of the ability of a conformational ensemble to explain the experimentally determined parameters is the χ^2 value:

$$\chi^2 = \sum_i \left(\frac{O_{i,\text{expt}} - O_{i,\text{calc}}}{\sigma_i} \right)^2 \tag{1.8}$$

in which O_i is the i:th NMR parameter as determined from either experiment or calculation as denoted by the subscript. The estimated uncertainties, σ_i, should reflect uncertainties in the predicted values as well as in the experimental values.

To the extent that the experimental parameters are sensitive to the conformational distribution, agreement with experiment is a rather demanding test of force field accuracy. Small errors in relative energy lead to large deviations in populations when conformations are of similar energy (Figure 1.8). For example, a difference of 1 kcal/mol in the free energy of two states leads to a population ratio 16:84 at 310 K. Comparatively, small changes in torsion angles typically lead to much larger energy changes.

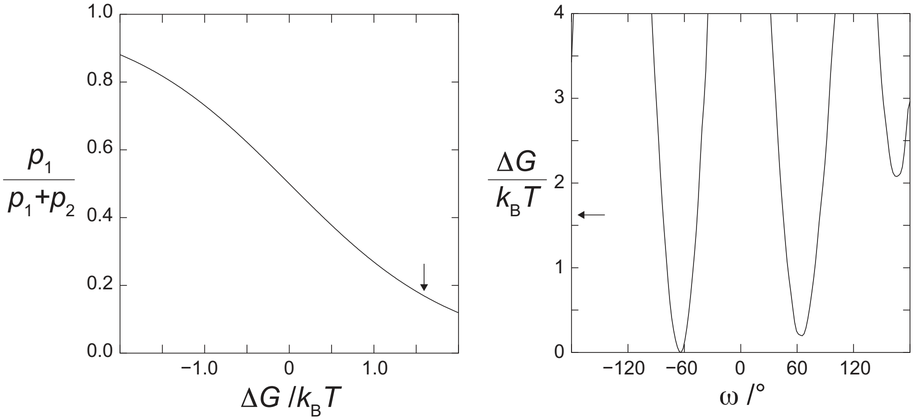

Figure 1.8: (*left*) Population of one state in a two-state equilibrium as a function of the energy difference to the other state. (*right*) Free energy as a function of the ω torsion angle in the trisaccharide in Chapter 4. The arrow indicates the point where ΔG equals 1 kcal/mol at 310 K.

Disagreement between parameters as predicted by MD simulations and as determined from experiment can of course come from incorrect populations as well as in the geometries of individual conformations. One of the major challenges in conformational analysis is determining the source of discrepancies and, if possible, to adjust the conformational ensemble accordingly.

1.5 Aims

In order to delineate the relationship between structure and function of carbohydrates, their behavior in solution must be well understood.

The aim of this work has been to advance the understanding of dynamic conformational properties of oligosaccharides in water, relying on the synergistic use of molecular dynamics simulations and NMR spectroscopy.

One goal was to suppress the influence of ${}^{1}J_{\mathrm{CC}}$s in the J-HMBC experiment in order to allow measurement of additional coupling constants in ^{13}C labeled compounds. The second project intended to observe hydroxyl protons under physiological conditions and to determine the extent and nature of hydrogen bonding in sucrose.

Several projects in this thesis aimed at determining the conformational preferences of various short oligosaccharide fragments. Discrepancies between simulations and experiments should guide improvements of carbohydrate force fields. Furthermore, it is likely that the conformational preferences of short oligosaccharides embody many of the driving forces that determine the conformations also for larger oligo- and polysaccharides.

2. J-HMBC: Suppressing Interference from ^{13}C Labeling (Paper I)

2.1 Background

The measurement of heteronuclear coupling constants gives access to a rich source of conformational information.[65–67] Used throughout the projects in this thesis, the J-HMBC[42] experiment is a particularly powerful method allowing the extraction of many heteronuclear long-range coupling constants from one single spectrum. The larger evolution time for coupling constants ($\kappa \times t_1$) than for chemical shifts (t_1) allows the combination of high resolution with respect to coupling constants with a large spectral window for chemical shifts.

Site-specific ^{13}C labeling facilitates the measurement of coupling constants involving the labeled carbon. Homonuclear ^{13}C,^{13}C and heteronuclear ^{13}C,^{1}H coupling constants can then be determined directly from splittings in 1D spectra or by total line-shape analysis.[68,69]

For carbon atoms directly bound to the ^{13}C label, as depicted in Figure 2.1, one-bond ^{13}C,^{13}C coupling constants will give rise to an additional splitting in the J-HMBC experiment, in many cases of comparable magnitude to the scaled heteronuclear coupling constants of interest. The superposition of the two types of splitting gives rise to confusing spectra in which the desired $^{n}J_{\mathrm{CH}}$ value is obscured.

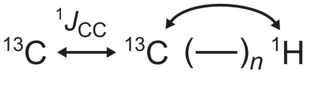

Figure 2.1: Schematic spin system showing the coupling partners involved. The coupling constant of interest is $^{n}J_{\mathrm{CH}}$ and the interference originates from $^{1}J_{\mathrm{CC}}$.

Two approaches frequently used for the suppression of undesired coupling constant evolution in two-dimensional NMR experiments are constant time elements[70] and frequency-selective pulses.[71] Thus, the aim of the current project was to suppress the evolution of ${}^1J_{\mathrm{CC}}$s in the J-HMBC experiment utilizing these two strategies.

2.2 Pulse programs

As a starting point, the pulse programs published by Meissner and Sørensen[42] were used. The two modifications allowing the suppression of ${}^1J_{\mathrm{CC}}$s are shown in Figure 2.2, representing the selective pulse and constant time strategies, respectively.[i] The sequence shown in Figure 2.2a, but without the selective pulse, will be referred to as the unmodified pulse sequence.

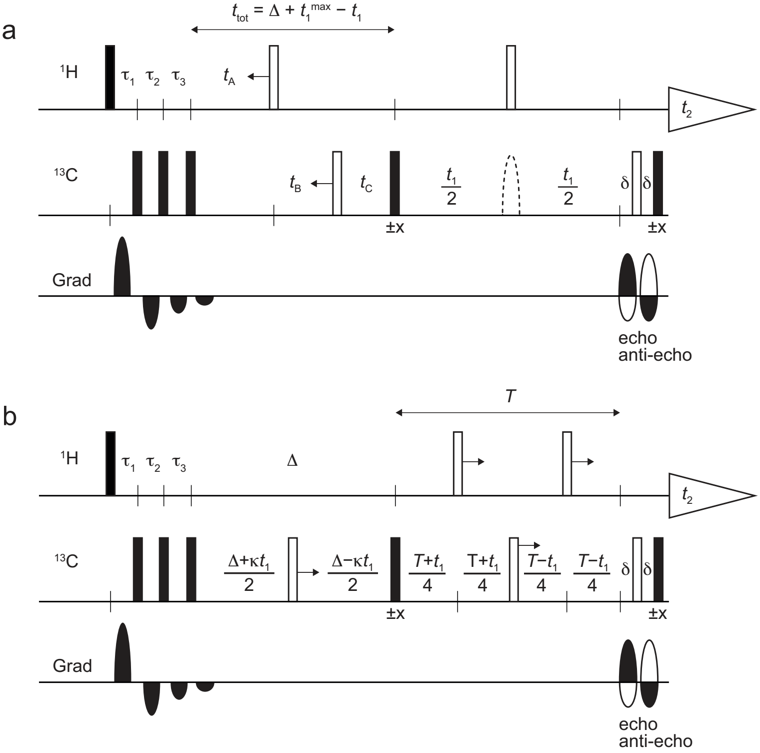
a
$t_{tot} = \Delta + t_1^{max} - t_1$
^{1}H
τ_1 τ_2 τ_3
t_A
t_2
^{13}C
t_B
t_C
$\frac{t_1}{2}$
$\frac{t_1}{2}$
δ δ
±x
±x
Grad
echo
anti-echo
b
T
^{1}H
τ_1 τ_2 τ_3
Δ
t_2
^{13}C
$\frac{\Delta+\kappa t_1}{2}$
$\frac{\Delta-\kappa t_1}{2}$
$\frac{T+t_1}{4}$
$\frac{T+t_1}{4}$
$\frac{T-t_1}{4}$
$\frac{T-t_1}{4}$
δ δ
±x
±x
Grad
echo
anti-echo

Figure 2.2: Pulse program modifications for the suppression of ${}^1J_{\mathrm{CC}}$s using a frequency-selective π pulse as indicated by a dashed ellipse in (a), or by the constant time element of length T in (b). Filled and hollow rectangles refer to non-selective $\pi/2$ and π pulses, respectively. For definitions of $\tau_{1,2,3}$ and $t_{\mathrm{A,B,C}}$, see reference 42.

---

[i] Note that the pulse sequence shown in Figure 2.2a is also a CT experiment, designed for the suppression of modulation by J_{HH}.

Introducing a selective π pulse at the center of the frequency evolution period as shown in Figure 2.2a leads to the refocusing of any scalar couplings between the nuclei affected by the pulse and those that are not.

When the use of a selective pulse is undesirable, the sequence in Figure 2.2b can be used instead, implementing a constant time element previously used in HMQC-type experiments.[72] The carbon chemical shift evolves during T as the carbon π pulse moves towards the end of the pulse program when t_1 is incremented, while evolution under homonuclear ^{13}C,^{13}C couplings remains constant and does not result in any t_1 modulation; hence the corresponding splittings are absent in the resulting spectra.

2.3 Experimental evaluation

In order to evaluate the performance of the two modified pulse programs, spectra were acquired for the site-specifically ^{13}C labeled oligosaccharides shown in Figure 2.3.

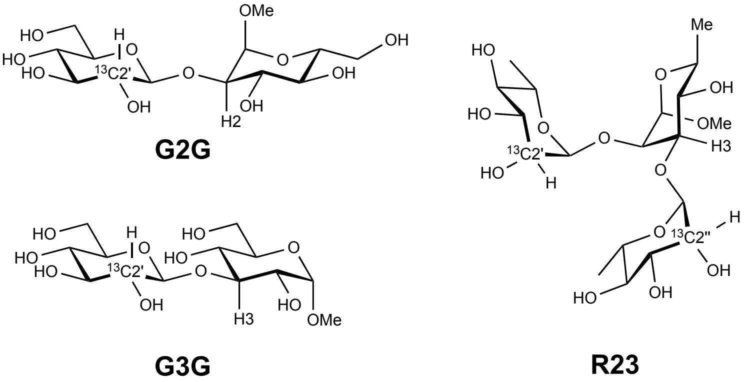

Figure 2.3: The three site-specifically ^{13}C-labeled oligosaccharides used to evaluate the pulse program modifications.

Due to the site-specific labeling at the 2' (and 2'') positions, one-bond couplings to C1' and C3' are observed, and hence the measurement of heteronuclear coupling constants involving these two carbons will be disturbed. The $^3J_{\mathrm{C1'},\mathrm{H}n}$ coupling constant is related to the glycosidic torsion angle ψ and is thus important for conformational studies.

The interference is apparent when using the original pulse sequence, as demonstrated for **G2G** in Figure 2.4. The spectrum in Figure 2.4a was obtained using a large scaling factor together with a high resolution in the indirect dimension. Both the desired anti-phase splitting ($\kappa\times{}^3J_{\mathrm{C1'},\mathrm{H2}}$)

and the disturbing in-phase splitting due to ${}^1J_{CC}$ are clearly visible. Using a smaller scaling factor results in a complicated peak pattern as shown in Figure 2.4c from which it is not straightforward to extract the desired coupling constant.

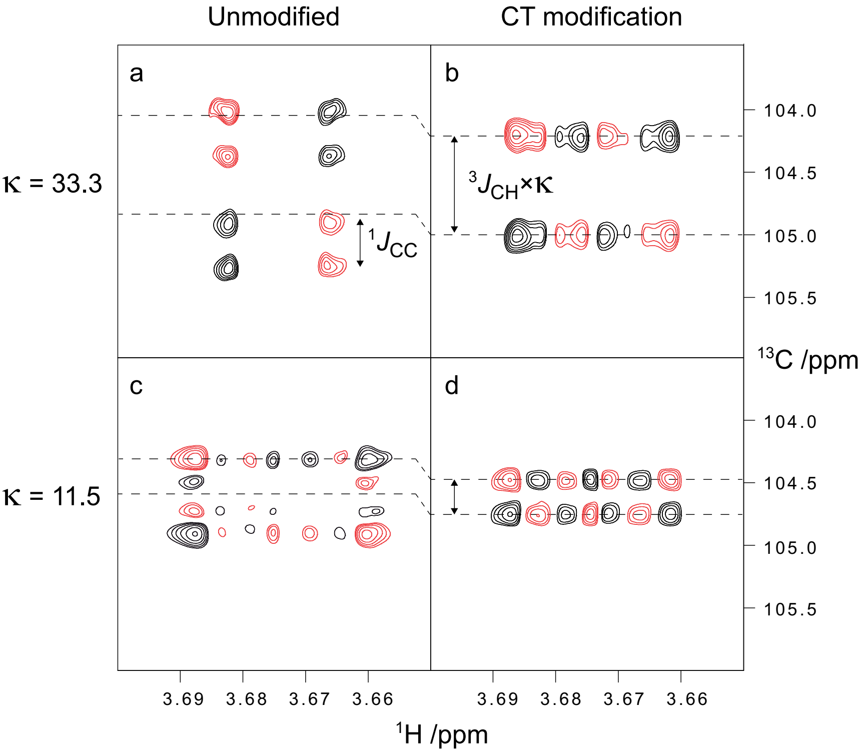

Figure 2.4: J-HMBC spectra obtained for [2'-^{13}C]-**G2G** using different scaling factors with the unmodified pulse sequence as well as the CT modified version shown in Figure 2.2b. The splitting due to ${}^3J_{C1',H2}$ is indicated by dashed lines.

The use of the constant time modification, shown in Figure 2.2b, reduces the complexity of the spectrum, allowing coupling constants to be accurately determined, as shown in Figures 2.4b and d.

The top trace in Figure 2.5 demonstrates that using the unmodified pulse sequence together with ^{13}C labeled **R23** gives broad and asymmetric peaks. This is due to a large contribution from the isotopologue having ^{12}C at the 2'' position, giving the same spectrum as the unlabeled compound. The reemergence of the expected doublet of doublet peak pattern in the difference between the projections from labeled and unlabeled **R23** is shown in the second trace (Δ) in Figure 2.5.

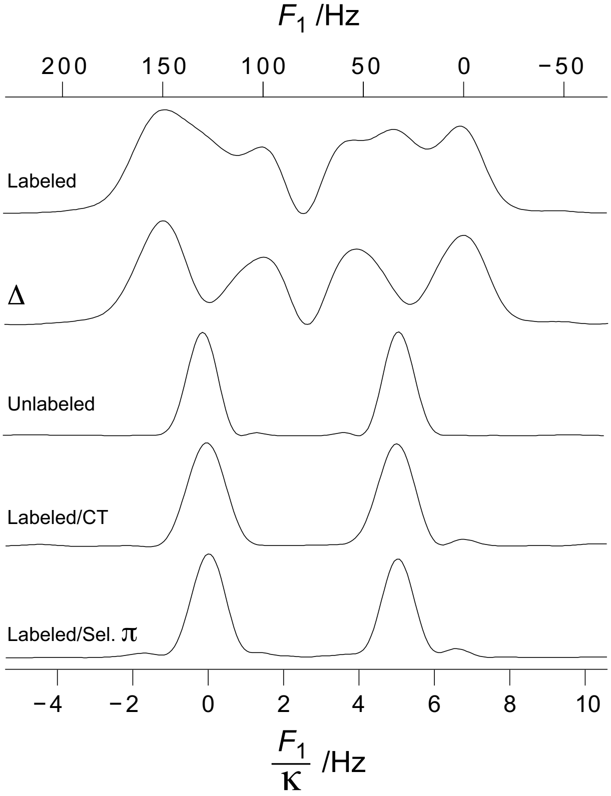

Figure 2.5: 1D projections of magnitude processed J-HMBC spectra obtained with $\kappa = 18.8$ for unlabeled and site-specifically ^{13}C labeled **R23** as indicated, showing the splitting relevant for $^3J_{\mathrm{C1}'',\mathrm{H3}}$. Δ shows the difference between the projections for the labeled and unlabeled compounds. The two lower projections were obtained using the CT modification and the selective π pulse modification, respectively.

The particular batch of **R23** used herein was found to contain more of the ^{12}C2'',^{13}C1'' isotopologue than expected from a completely selective labeling.[73] As seen from Figure 2.6, this type of contamination is also present for **G2G** but to a smaller extent as determined from the relative heights of doublet and singlet peaks for the anomeric carbons. Using either of the proposed pulse sequence modifications leads to the desired simple doublet peak shape shown in the two lower projections in Figure 2.5, similar to that observed for unlabeled **R23**.

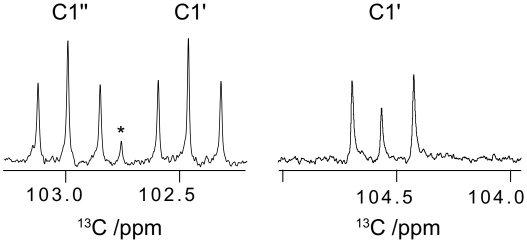

Figure 2.6: 1D ^{1}H-decoupled ^{13}C spectra for **R23** (*left*) and **G2G** (*right*), showing the anomeric carbons which are adjacent to the ^{13}C label. The asterisk denotes an impurity.

In all cases, the heteronuclear ^{13}C,^{1}H long-range coupling constants determined using the site-specifically labeled compounds together with these modified pulse sequences were in excellent agreement with reported values.[73,74] Spectral simulation with minimal spin systems reproduced the interference from $^1J_{\mathrm{CC}}$ when using the unmodified sequence as well as the clarification achieved by the modified sequences (cf. Figure 4 in Paper I).

2.4 Conclusions

Two approaches were evaluated and found to solve the problems occurring when applying the J-HMBC experiment for the determination of heteronuclear long-range coupling constants in site-specifically ^{13}C labeled compounds. The source of the interference was shown to be homonuclear ^{13}C,^{13}C couplings. By their suppression, the J-HMBC experiment can be used to accurately measure heteronuclear long-range coupling constants involving carbon nuclei adjacent to a ^{13}C labeled position.

Although not tested in this project, it should be possible to apply the pulse sequence with the constant time modification shown in Figure 2.2b to randomly ^{13}C enriched compounds, thus allowing the rapid and sensitive determination of several heteronuclear ^{13}C,^{1}H long-range coupling constants in a single sample.

3. Hydrogen Bonding in Sucrose: Experimental Evidence and MD Simulations (Paper II)

3.1 Background

Being the most abundant disaccharide on earth, sucrose, α-D-Glc$p$-(1$\leftrightarrow$2)-β-D-Fru$f$ (Figure 3.1), has received considerable scientific attention over the past century. Among the prominent features of this molecule is its sweet taste, motivating its widespread use in food products. The crystal structure was solved completely in 1973 (Figure 3.1b),[75] and subsequently efforts were directed towards determining the conformation in solution. Early studies supported a rigid conformation close to the one found in the crystal structure,[76,77] but this was later disputed in favor of a structure with more flexibility in the glycosidic linkages.[78–82] A recent study using MD simulations together with RDCs and scalar coupling constants found that the crystal structure conformation is the most populated one in solution, with limited flexibility associated mostly with the $\psi_{\mathrm{O}5f}$ torsion angle.[83]

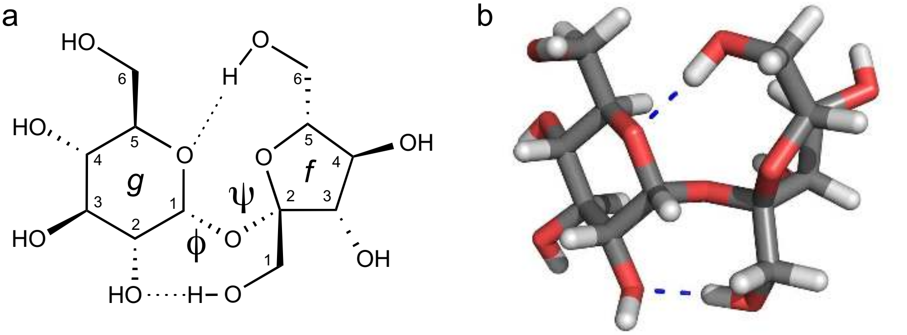

Figure 3.1: (a) Schematic representation of sucrose with the numbering and lettering convention used. (b) Structure determined by crystal neutron diffraction with intramolecular hydrogen bonds indicated by blue dashes.[75]

Two intramolecular hydrogen bonds were found in the crystal structure, viz. O2*g*$\cdots$HO1*f* and O5*g*$\cdots$HO6*f* (Figure 3.1). Their fate upon immersion in water has been the topic of several investigations. The temperature dependence of chemical shifts, scalar coupling constants, and exchange rates for the hydroxyl hydrogens in water/acetone mixtures, do not support any persistent intramolecular hydrogen bonding.[84] However, the observation of a ROESY exchange peak between HO1*f* and HO2*g* in supercooled water supports the transient presence of a hydrogen bond.[85]

The use of acetone or supercooled conditions were required due to the rapid exchange with solvent protons, making hydroxyl protons invisible in water solution. However, the use of conditions far from physiological might alter conformational equilibria and it is therefore desirable to perform experiments in a less artificial environment.

The detection of hydroxyl protons gives access to additional NMR parameters for use in conformational studies, including direct detection of hydrogen bonding. The presence of an intramolecular hydrogen bond is a particularly useful indicator of conformation.[86] In this project the aim was to find suitable conditions for the detection of hydroxyl protons at room temperature in water for sucrose and trehalose and to investigate hydrogen bonding directly.

3.1.1 Direct detection of hydrogen bonds

Varying ionic strength and pH led to the finding of optimal conditions for the detection of hydroxyl protons. Using deionized water with pH 6.5, it was possible to reach higher temperatures (up to 298 K for trehalose and 283 K for sucrose) and lower concentrations (50 mM) than previously reported. Hydroxyl resonances were assigned using the HSQC-TOCSY[87] experiment with a short isotropic mixing time (10 ms). Extending the mixing time to 30 ms gave correlations over hydrogen bonds via ${}^{3h}J_{\mathrm{HO,HC}}$s. This allows the determination of hydrogen bond directionality; a cross peak will have the carbon shift of the acceptor (HC–O) and the hydroxyl proton shift of the donor (H–O). Using this method, hydrogen bonds were shown to occur between O2*g* and HO1*f*, and between O1*f* and HO2*g*, i.e. as found in the crystal structure as well as with the reverse directionality. Interresidual hydrogen bonding involving HO6*f* was not detected. This does not exclude that such bonding is present; small coupling constants (${}^{3h}J_{\mathrm{HO6}f,\mathrm{H5}g}$ or ${}^{3h}J_{\mathrm{HO6}f,\mathrm{H1}g}$) can be caused by the hydrogen bond geometries. For the same reason, it is not possible to compare the amounts of different hydrogen bonds.

At concentrations higher than 400 mM a hydrogen bond to O3*f* from either HO3*g* or HO4*g* was detected. Due to the very small chemical shift difference between these two donors, it was not possible to deduce which of these contribute to the observed peak. It is obvious from Figure 3.1 that these bonds cannot occur in the shown conformation; the distance between the oxygen atoms is 6.2 Å for both cases. In comparison, the O$\cdots$O distances for the two hydrogen bonds shown are approximately 2.8 Å. Thus, either the hydrogen bond occurs in another conformation, or it is an intermolecular hydrogen bond. The observed peak volume has an approximately quadratic dependence on the sucrose concentration, suggesting that the hydrogen bond is intermolecular. The peaks corresponding to the hydrogen bonds between O2*g* and O1*f* have approximately linear relationships as expected for intramolecular hydrogen bonds.

One of objectives in following modeling studies was to determine whether either of the two possible O3*f*$\cdots$HO3/4*g* hydrogen bonds could be accommodated intramolecularly. Additionally the nature and extent of intermolecular hydrogen bonding in aqueous solution was investigated, especially with respect to the O3*f*$\cdots$HO3/4*g* hydrogen bonds.

3.2 Molecular modeling

3.2.1 Restrained Langevin dynamics

As a computationally inexpensive way to find possible conformations allowing for hydrogen bonding to occur between O3*f* and either HO3*g* or HO4*g*, Langevin dynamics simulations were performed with a 10 kcal/mol restraint applied to either the O3*f*–O3*g* distance or the O3*f*–O4*g* distance (3.2 Å). Neither of the simulations satisfied the distance criteria, with average distances being 3.9 Å and 3.6 Å, respectively, for the two simulations. The average energy was 9.5 and 6.7 kcal/mol higher than for an unrestrained simulation, with approximately 2 kcal/mol from the restraint term; the rest is largely accounted for by distortions to the ring geometry and glycosidic torsion angles (Figure 3.2). From this analysis, it is unlikely that an intramolecular O3*f*$\cdots$HO3/4*g* hydrogen bond is present.

3.2.2 MD simulations at different concentrations

In order to investigate the possibility of an intermolecular explanation for the O3*f*$\cdots$HO3/4*g* hydrogen bond, an array of MD simulations at 283 K was performed with different concentrations ranging from 0.13 M to 1.3 M. As starting geometries, crystals containing 2–20 sucrose molecules were built using neutron diffraction data[75] and placed in water boxes.

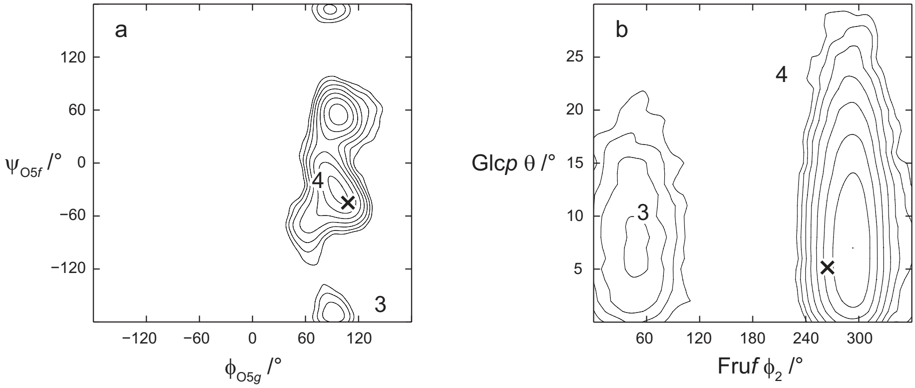

Figure 3.2: The PMF from an aqueous MD simulation of sucrose at $c = 0.128$ M in levels of k_BT as a function of the glycosidic torsion angles (a) and as a function of the ring puckering phases[88] in the two residues (b). The × shows the values for crystalline sucrose, while the average values from restrained LD simulations are denoted by 3 and 4, indicating the number of the oxygen in the glucose residue involved in the restraint.

The dissolution and subsequent equilibration was monitored by means of sucrose-sucrose distance distribution functions as well as by the number of intermolecular hydrogen bonds between sucrose molecules (Figure 3.3a).

For small crystal sizes (2 and 4 sucrose molecules), dissolution was complete within a few hundred ps while the largest crystal size (20 sucrose molecules) still showed signs of structuring after 5 ns. The number of intermolecular hydrogen bonds between sucrose molecules drops during the same time and reaches a stable value around which fluctuations occur throughout the simulation, as shown in Figure 3.3a.

Intermolecular hydrogen bonding

An approximately quadratic relationship was found between the number of intermolecular hydrogen bonds and the number of sucrose molecules in the simulation, as shown in Figure 3.3b. For the simulation at the highest concentration there was, on average, approximately one intermolecular hydrogen bond per sucrose molecule, with 84% of the sucrose molecules being involved in at least one such hydrogen bond.

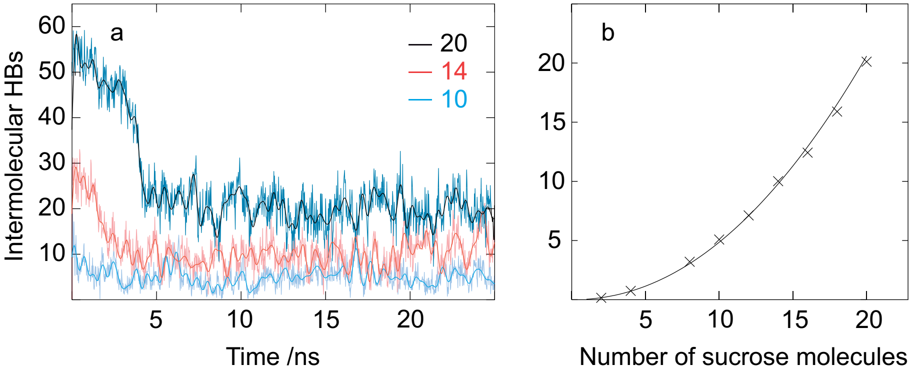

Figure 3.3: (a) Number of intermolecular hydrogen bonds between sucrose molecules as a function of time for simulations with 10, 14, and 20 sucrose molecules. (b) Equilibrium average number of intermolecular hydrogen bonds (×) as a function of the number of sucrose molecules in the simulations. The line is a fitted power equation: $0.04x^{2.08}$.

Intermolecular hydrogen bonds were classified by their donor and acceptor atoms. By fitting a quadratic function to the concentrations of each type of hydrogen bond and the concentrations of sucrose, equilibrium constants were obtained for the following type of equilibria:

$$\text{Sucrose} + \text{Sucrose} \rightleftharpoons \text{H-bond} \tag{3.1}$$

$$K_{\text{hb}} = \frac{[\text{H-bond}]}{[\text{Sucrose}]^2} \tag{3.2}$$

The resulting equilibrium constants were analyzed to determine if there were any preferred donor/acceptor pairs. As can be seen from Figure 3.4, the acetal oxygen atoms (O5*f*, O5*g* and O1*g*) were least likely to participate in intermolecular hydrogen bonding. The most frequent acceptors were the primary oxygens (O1*f*, O6*f* and O6*g*). Among the ten most frequent intermolecular hydrogen bonds, shown in Table 3.1, seven involve a primary oxygen atom as an acceptor. The three other bonds all involve O3*g*, namely; O3*f*· · ·HO3*g*, O3*g*· · ·HO4*f*, and O3*g*· · ·HO3*g*.

From NMR spectroscopy, a hydrogen bond donated to O3*f* from HO3*g* and/or HO4*g* was observed. It is encouraging that one of these is indeed among the most frequent intermolecular hydrogen bonds in the simulation, and suggest that O3*f* prefers HO3*g* (Figure 3.5) over HO4*g* as the donor. However, it should be noted that 92% of all possible hydroxyl-hydroxyl hydrogen bonds have K_{hb} values higher than half of the maximum, and there is no clear-cut distinction between the various hydrogen bonding arrangements (Figure 3.6).

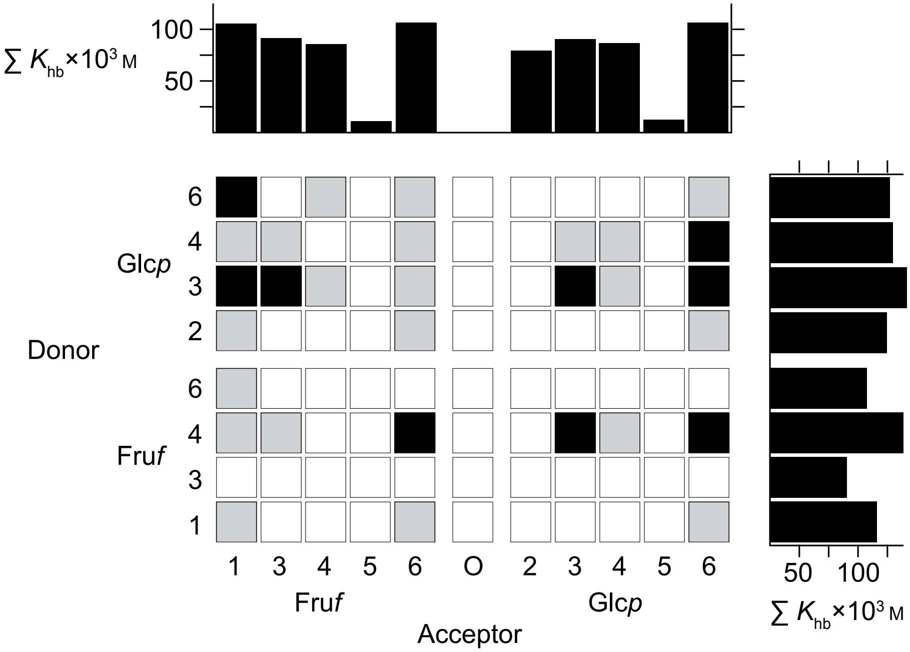

Figure 3.4: Hydrogen-bond equilibrium constants for all donor/acceptor pairs. Black: above 90%, grey: 90% – 75% and white: less than 75% of the maximum value ($16\times10^{-3}\text{M}^{-1}$).

Table 3.1: Hydrogen bond equilibrium constants. The standard error in the last decimal is given in parentheses.

Donor	Acceptor	$K_{\text{hb}} \times 10^3/\text{M}^{-1}$
4*f*	6*f*	16.0(4)
4*f*	6*g*	15.8(7)
4*g*	6*g*	15.4(4)
3*g*	**3*f***	15.3(4)
3*g*	6*g*	15.2(5)
4*f*	3*g*	15.1(6)
3*g*	3*g*	15.0(5)
6*g*	1*f*	15.0(5)
3*g*	1*f*	14.7(5)
6*g*	6*f*	14.3(5)
.	.	.
4*g*	**3*f***	12.8(9)

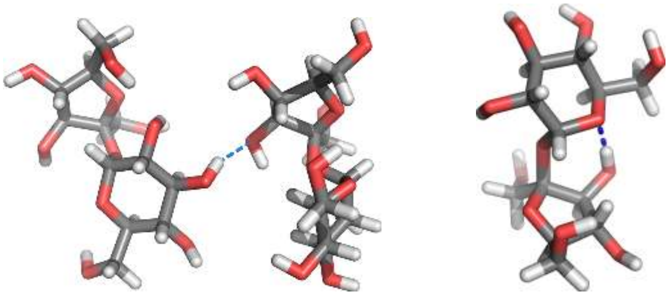

Figure 3.5: Snapshots from the simulation at $c = 1.3$ M showing the intermolecular O3$f\cdots$HO3g hydrogen bond (*left*) and the intramolecular O5$g\cdots$HO3f hydrogen bond (*right*).

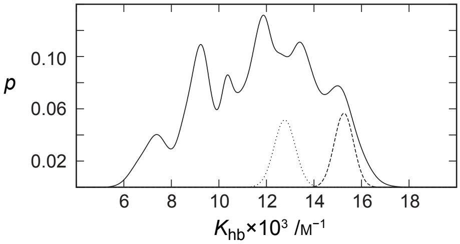

Figure 3.6: Histogram for K_{hb} values, for the 64 values that were above $4{\times}10^{-3}\mathrm{M}^{-1}$. Each value has been broadened by the standard error of the fit. The contributions from O3$f\cdots$HO3g (dashes) and O3$f\cdots$HO4g (dots) are magnified five times.

Intramolecular hydrogen bonding

Although it could be the case that intramolecular hydrogen bonding would be affected by concentration, no significant trends could be determined from the MD simulations. The main hydrogen bonds present were O5$g\cdots$HO3f (27%) O2$g\cdots$HO1f (14%), O5$g\cdots$HO6f (9%), and O6$f\cdots$HO6g (8%). These were confined to conformations resembling the one found in the crystal, with the exception being the O5$g\cdots$HO3f hydrogen bond (Figure 3.5) which was only present when $\psi_{\mathrm{O5}f}$ had values around +60° (Figure 3.7). The low amount of intermolecular hydrogen bonds having HO3f as the donor atom (Figure 3.4) is likely caused by the large amount of the intramolecular O5$g\cdots$HO3f hydrogen bond.

Comparison with NMR spectroscopy

Figure 3.8 shows the amount of hydrogen bonding in MD simulations compared to the cross-peak intensities from NMR spectroscopy. The dependency on concentration is similar in both experiment and simulation; intramolecular hydrogen bonds have a close to linear relationship to concentration with exponents from experiment equal to 1.2 and 1.0 for O2$g\cdots$HO1f and O1$f\cdots$HO2g, respectively. From simulation, the exponents are 1.0 and 1.3, respectively, for the two intramolecular

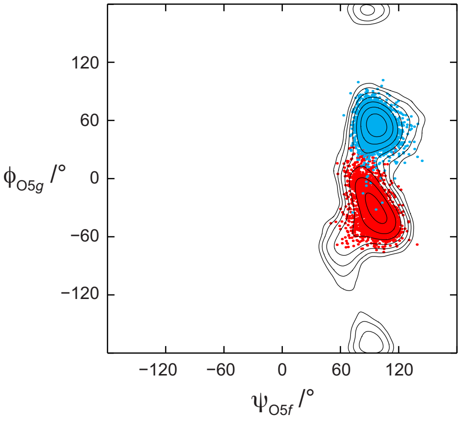

Figure 3.7: The PMF as a function of ψ_{O5f} and ϕ_{O5g} together with the values of the same torsion angles when the intramolecular hydrogen bonds O5$g\cdots$HO3f (blue) and O2$g\cdots$HO1f (red) were present.

hydrogen bonds. On the other hand, the intermolecular O3$f\cdots$HO3g hydrogen bond has a near-quadratic relationship with the exponent 1.9 from experiment and 2.1 from simulation.

The O2$g\cdots$HO1f hydrogen bonding arrangement is favored over the reverse directionality by a factor of seven in the MD simulation. However, the corresponding cross-peak intensities are essentially equal from NMR spectroscopy, suggesting that other factors than occupancy affect the amount of magnetization transfer.

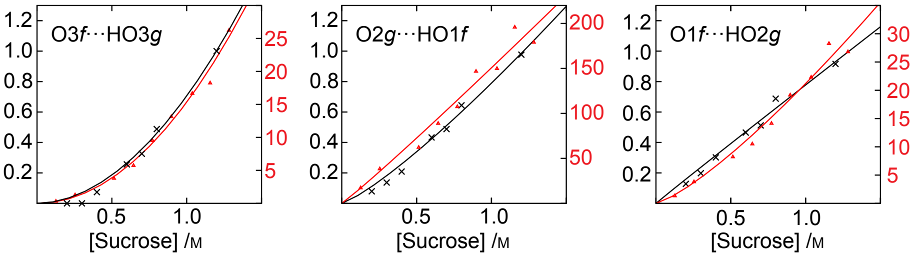

Figure 3.8: Concentration dependence of normalized cross-peak intensity from NMR spectroscopy (black) and hydrogen bond concentrations from MD simulations (red, mM). Lines were obtained by fitting an equation of the form $y = a \times [\text{Sucrose}]^b$ to the data points.

3.3 Conclusions

By lowering the ionic strength of the solvent and using a pH value of 6.5, hydroxyl hydrogens in sucrose and trehalose were observable at lower concentrations and at higher temperatures than previously attainable. Hydroxyl protons were possible to assign through isotropic mixing, and hydrogen bonding (including directionality) was observed via scalar coupling. One of the two intramolecular hydrogen bonds present in the crystal structure was confirmed to persist in solution, as well as with the donor/acceptor roles reversed.

The lack of reasonable intramolecular O3$f\cdots$HO3/4g hydrogen bonding geometries suggests that the cross-peak observed by NMR spectroscopy arises from an intermolecular interaction. The quadratic concentration dependency of the intensity of the corresponding peak supports an intermolecular interaction, as does the observation that these interactions occur frequently in the MD simulations. Although the hydrogen bond from HO3g is slightly favored over that from HO4g in the MD simulations, it is not possible to confidently discriminate between these two hydrogen bonding arrangements.

Intermolecular hydrogen bonding was not found to be particularly selective in the MD simulations. Whether this is also the case in real solutions of sucrose remains to be determined. That only O3$f\cdots$HO3/4g is experimentally observed could indicate that it is preferred over other intermolecular hydrogen bonds. However, it cannot be excluded that other intermolecular hydrogen bonds are present but are not detected. For example, the corresponding coupling constants when the hydrogen bonds are present could differ for other geometric reasons.

4. Conformation of a Central Trisaccharide in Le^{a}Le^x (Paper III)

4.1 Background

Carbohydrate patterns displayed specifically by tumor cells are potential targets for the development of treatments as well as diagnostic tools.[89,90] The hexasaccharide Le^{a}Le^x (Figure 4.1) is expressed at the surface of cells of squamous carcinoma of the lung.[91] Antibodies have been isolated from mice after immunization using such cells and these were found to bind selectively to the Le^{a}Le^x hexasaccharide and only weakly to the Le^a trisaccharide. This distinction is important since the Le^a fragment is frequently presented on healthy cells,[92] and cross-reactive antibodies from vaccination would likely elicit an autoimmune response.

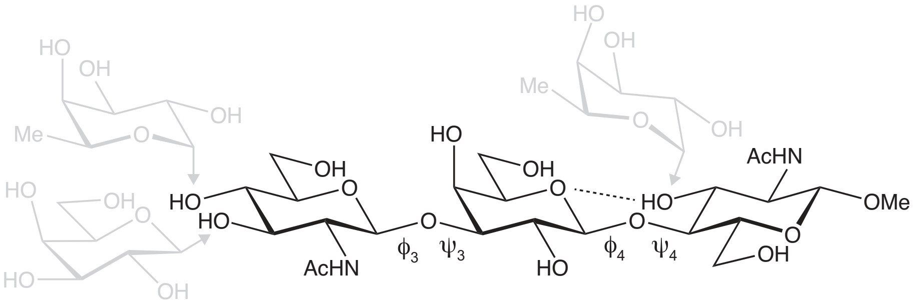

Figure 4.1: The studied trisaccharide (black) with dashes indicating a persistent hydrogen bond. Additional residues in the full Le^{a}Le^x hexasaccharide are indicated in gray.

In order to develop a vaccine specifically targeting tumor cells, it is desirable to have an antigen which provokes immunization against the full Le^{a}Le^x hexasaccharide but not against any native carbohydrate structures. It was hypothesized that the selective antibodies mentioned above recognize an internal epitope not present in either of the Le^a (left part in Figure 4.1) or Le^x (right part) trisaccharides. Therefore, our collaborators in the group of F-.I. Auzanneau set out to synthesize small fragments of the full hexasaccharide and investigate their conformational behavior. As a part of these studies, the trisaccharide α-L-Fuc*p*-(1→4)-β-D-Glc*p*NAc-(1→3)-β-D-Gal*p*-OMe was investigated and found to show conformational exchange at the (1→3)-linkage.[93]

Related structures containing the β-D-Glc*p*NAc-(1→3)-β-D-Gal*p* motif have previously been studied. For example, a single conformation was found for this linkage in the human milk pentasaccharide LNF-2.[94] On the other hand, conformational exchange at the β-D-Glc*p*NAc-(1→3)-β-D-Gal*p* linkage has been shown for LNF-1[63,95] and for LNnT.[96] The Le^a trisaccharide[97–99] and the Le^x trisaccharide[99,100] have been investigated previously and found to have single conformations in solution.

In this study, the trisaccharide segment β-D-Glc*p*NAc-(1→3)-β-D-Gal*p*-(1→4)-β-D-Glc*p*NAc-OMe, shown in Figure 4.1, was investigated using MD simulations. Comparisons are made between three different force fields, and with NMR spectroscopy.

4.2 MD simulations

Three MD simulations were performed using the GLYCAM06,[57] the PARM22/SU01[54] and the CHARMM2011[56] force fields. The former simulation was performed at 300 K for 20 ns while the two latter were performed at 280 K for 400 ns and 200 ns, respectively. The probability distributions for the glycosidic torsion angles in the simulation using the CHARMM2011 force field is shown in Figure 4.2.

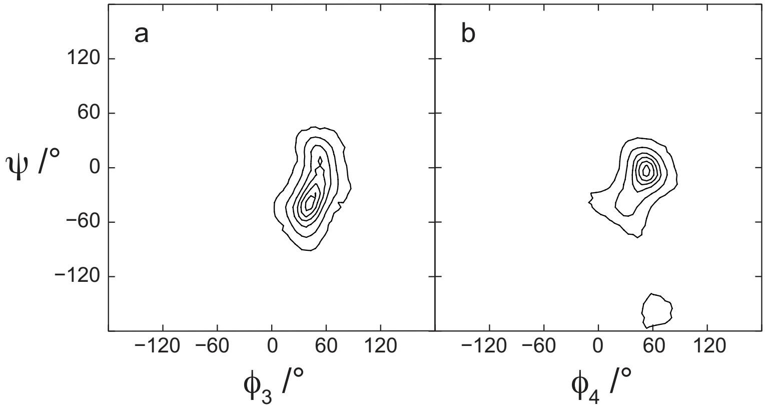

Figure 4.2: Probability density maps for the glycosidic torsion angles at the (1→3)-linkage (a) and at the (1→4)-linkage (b) using the CHARMM2011 force field with contours enclosing areas with higher than 90%, 70%, 50%, 30%, 10%, and 1%, respectively, of the maximum probability.

In all cases, the β-D-Gal$p$-(1→4)-β-D-Glc$p$NAc linkage was found to have a single preferred conformation with ϕ_4 being approximately 48° and with ψ_4 close to 0°. This is similar to the conformation found for the corresponding disaccharide more than 30 years ago using the simple HSEA force field.[97] This conformation is stabilized by a hydrogen bond between O5' and HO3, which was present to 37% in the PARM22/SU01 simulation and 41% in the CHARMM2011 simulation. In the PARM22/SU01 simulation the non-*exo*-anomeric conformation having $\phi_4 = -60°$, was briefly visited during the simulation; this will be discussed further in Chapter 5. When using the CHARMM2011 force field, a small fraction of the simulation time was spent in a state defined by $\psi_4 = 157°$.

The largest difference between the force fields was in their representation of ψ_3 torsion angle in the β-D-Glc$p$NAc-(1→3)-β-D-Gal$p$ linkage. In all cases, there was rapid conformational exchange at the ψ_3 torsion angle resulting in a bimodal population distribution as shown in Figure 4.3a, while maintaining a value of ϕ_3 close to 43°. However, the separation of these two conformations was found to differ between the force fields, with the PARM22/SU01 force field showing the largest separation while the CHARMM2011 force field had almost coalesced peaks for the two states. In addition, the GLYCAM06 force field also featured a single excursion lasting 3 ns to a conformation having $\psi_3 = 163°$.

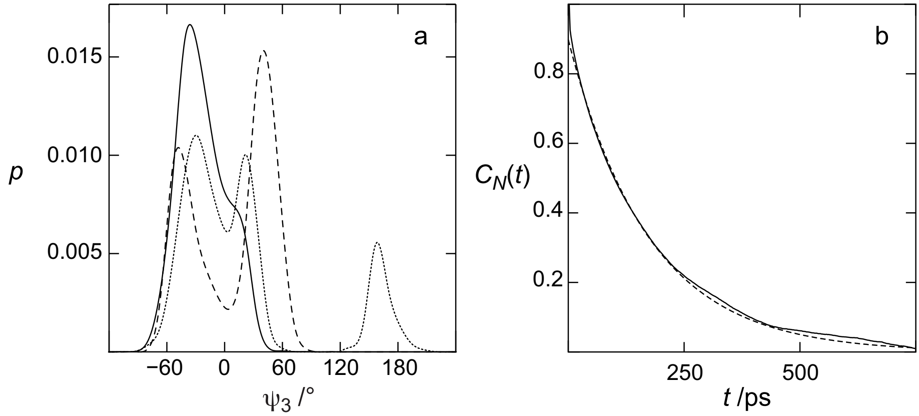

Figure 4.3: (a) Probability distribution functions for the ψ_3 torsion angle using the CHARMM2011 (lines), PARM22/SU01 (dashed) and GLYCAM06 (dots) force fields. (b) Number correlation function calculated for the ψ_3 torsion angle in the PARM22/SU01 simulation and the exponential fit (dashed).

The time scale for conformational interchange at the ψ_3 torsion angle in the PARM22/S01 simulation was investigated using a number correlation function,[101] shown in Figure 4.3b. Through fitting of a monoexponential decay to this function the correlation time was established to be 173 ps, which is slightly slower than the isotropic reorientational correlation time, $\tau_c \approx 100$ ps, calculated from the translational diffusion constants in the simulations.

4.3 Comparison with NMR spectroscopy

The conformational distributions from the MD simulations were used to calculate the NMR parameters available from experiment (Table 4.1). Overall, experimental values agree well with those calculated from the simulations, with the GLYCAM06 simulation giving smaller deviations for the (1→3)-linkage and CHARMM2011 performing better for the (1→4)-linkage.

The good agreement between calculated and experimentally determined values for the coupling constants related to ϕ_3 and ϕ_4 supports the finding that these torsion angles mainly reside in conformations stabilized by the *exo*-anomeric effect.

The largest part of the χ^2 value related to the (1→4)-linkage comes from the very short distance between H1' and H4 (2.16 Å) observed in NOESY experiments which is at least 0.13 Å longer in all of the MD simulations. However, a short distance is in qualitative agreement with an *exo*-anomeric conformation for ϕ_4 and values close to 0° for ψ_4.

The available experimental parameters related to the ψ_3 torsion angle are displayed in Figure 4.4 together with their angular dependencies as determined from either a Karplus-type equation[38] or from MD simulations, neglecting any differences in ϕ_3. Although the effective distance between H1'' and H3' is slightly shorter from MD simulations at $\psi_3 = -30°$, a single rigid conformation with this value could explain all available experimental parameters.

Taking librational motion into account reduces the H1''–H4' distance by ca. 0.2 Å as deduced by calculating the effective distance for a normal distribution with a standard deviation of 15° centered at $\psi_3 = -30°$. The deviation from experimental parameters as a function of ψ_3 was calculated assuming such fluctuations around a single value, reaching a minimum ($\chi^2 = 0.52$) at $\psi_3 = -25°$ as shown in Figure 4.5a. The relationships between effective distances and ψ_3 were obtained as weighted averages from the three simulations. While the value of ϕ_3 has an influence on these distances, this torsion angle was assumed to be adequately represented in this calculation.

Table 4.1: NMR parameters from experiment and MD simulations. Distances are in Å and coupling constants are in Hz.

Torsion angle(s)	Parameter	GLYCAM06	SU01	CHARMM2011	Expt.
ϕ_3, ψ_3	$r_{\mathrm{H1''-H3'}}$	2.39	2.42	2.24	2.29
ϕ_3, ψ_3	$r_{\mathrm{H1''-H4'}}$	3.20	3.25	3.07	3.34
ϕ_3	$^3J_{\mathrm{C3',H1''}}$	4.09	3.89	3.79	4.21
ψ_3	$^3J_{\mathrm{C1'',H3'}}$	5.03	3.64	4.47	4.73
	χ^2	1.2^a	3.4	2.4	
ϕ_4, ψ_4	$r_{\mathrm{H1'-H4}}$	2.36	2.34	2.29	2.16
ϕ_4	$^3J_{\mathrm{C4,H1'}}$	3.65	3.25	3.49	3.78
ψ_4	$^3J_{\mathrm{H1',C4}}$	5.80	5.79	5.58	$-^b$
	χ^2	2.4	2.4	1.2	

[a] Estimated uncertainties for experimental distances are 6% and for J-couplings 0.75 Hz.

[b] Not determined.

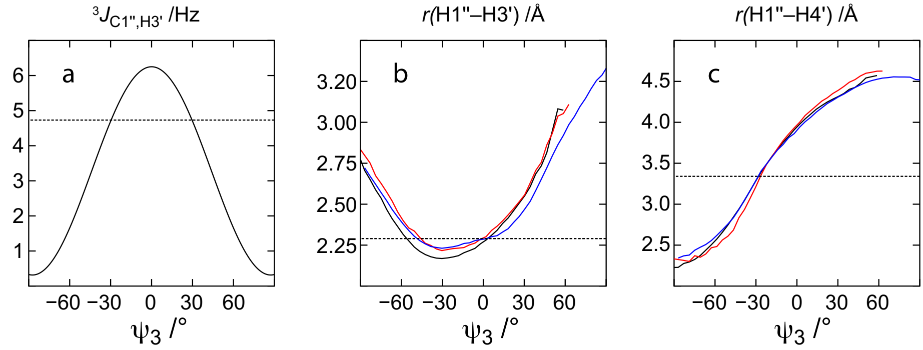

Figure 4.4: NMR parameters related to ψ_3; $^3J_{\mathrm{C1'',H3'}}$ (a) and the effective distances for H1''–H3' (b) and for H1''–H4' (c). Experimental values are indicated by dashed lines. For distances the different colors indicate to the force field used in the MD simulation; CHARMM2011 (black), PARM22/SU01 (blue) and GLYCAM06 (red).

In principle two or more conformations could be contributing to the observed values. This possibility is supported by the observation of conformational exchange involving ψ_3 in MD simulations using all three force fields. Additional support comes from previous studies of the β-D-Glc*p*NAc-(1→3)-β-D-Gal*p* linkage in similar molecules, as mentioned in the background to this chapter.

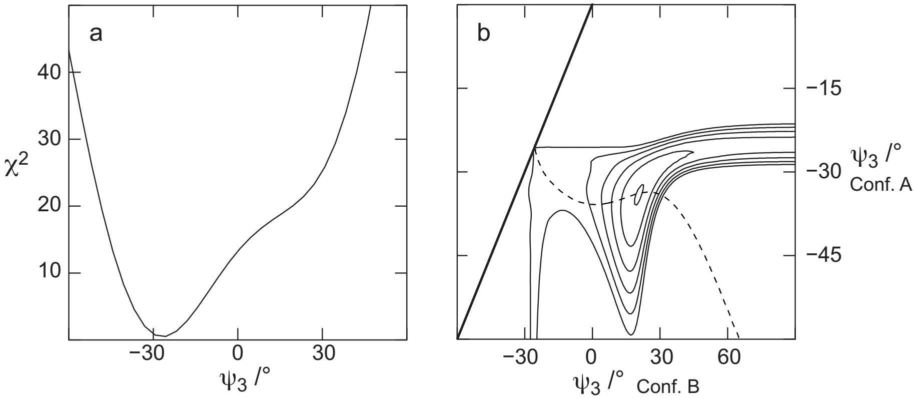

Figure 4.5: (a) χ^2 as a function of ψ_3 assuming a single conformation. (b) Optimization of χ^2 by adjusting the population of two conformations having different ψ_3. Note that only the part where $\psi_3^{\mathrm{B}} > \psi_3^{\mathrm{A}}$ is shown. Contours enclose areas having χ^2 less than 100%–20% in steps of 20%, and 1% of the minimum in (a). Solutions above the dashed line have more than 60% of conformation A and those below have less.

Indeed, the χ^2 value has a minimum ($\chi^2 = 0.0$) for a two-state equilibrium having $\psi_3^{\mathrm{A}} = -33°$ and $\psi_3^{\mathrm{B}} = 20°$ in a 60:40 ratio (Figure 4.5b). As the error is small already for the single state solution and three degrees of freedom are needed to fit a two-state equilibrium, additional NMR parameters have to be determined in order to resolve this uncertainty, e.g. homonuclear carbon-carbon coupling constants (viz. ${}^3J_{\mathrm{C1}'',\mathrm{C2}'}$ and ${}^3J_{\mathrm{C1}'',\mathrm{C4}'}$). However, it can be noted that the wide separation of the two ψ_3 conformations ($\psi_3^{\mathrm{B}} \approx 40°$ and $\psi_3^{\mathrm{A}} \approx -40°$) seen in the PARM22/SU01 simulation does not give good agreement with experimental parameters at any population ratio (cf. Figure 4.5b). It is likely the separation of these two states is smaller, as seen in the two other force fields.

4.4 Conclusions

MD simulations using three different force fields suggest that the trisaccharide β-D-Glc*p*NAc-(1→3)-β-D-Gal*p*-(1→4)-β-D-Glc*p*NAc-OMe in solution adopts an extended conformation with limited flexibility in the glycosidic torsion angles. For all force fields, the β-D-Gal*p*-(1→4)-β-D-Glc*p*NAc linkage shows limited fluctuations around the conformation defined by $\phi_4 \approx 48°$ and $\psi_4 \approx 0°$, stabilized by the *exo*-anomeric effect and by a persistent $\mathrm{O5'} \cdots \mathrm{HO3}$ hydrogen bond.

At the β-D-Glc*p*NAc-(1→3)-β-D-Gal*p* linkage, the three force fields agree to the extent that ϕ_3 is in the *exo*-anomeric conformation having $\phi_3 = 43°$ and that there are at least two conformations in exchange at the ψ_3 torsion angle. The latter torsion angle is where the major differences between the force fields are found; the PARM22/SU01 simulation predicts two states separated by approximately 80° while for the CHARMM2011 simulation the two states are barely separated. An intermediate situation is found in the GLYCAM06 simulation, i.e., a narrower separation than found in the former simulation, but more pronounced than in the latter.

While the experimental parameters do not exclude the possibility of flexibility at the β-(1→3)-linkage, they can be rationalized assuming only a single conformation, and additional parameters would have to be determined in order to rule out either of these cases. A wide separation between the two conformations at the ψ_3 torsion angle, as found in the PARM22/SU01 force field, is not able to explain the observed parameters, regardless of their relative proportions.

It is encouraging that the conformational descriptions provided by the two more recent force fields (viz. GLYCAM06 and CHARMM2011) are the ones more consistent with experiment; although they are not perfect, they perform better than the decade-old PARM22/SU01 force field.

The possibility of conformational exchange is likely to also apply to the full $\mathrm{Le^aLe^x}$ hexasaccharide, suggesting that it could be possible for antibodies to recognize specifically the topologies presented in one of the conformations but not in the other, and vice versa.

5. Involvement of the *N*-Acetyl Group in Glycosidic Conformation (Papers III and IV)

5.1 Background

The *N*-acetyl substituent appears deceptively small as simply 'AcNH' in schematic representations. Figure 5.1 shows that in fact this group contributes significantly to the size of a monosaccharide residue and provides possibilities for polar interactions with its amide hydrogen and oxygen and for hydrophobic and steric interactions with the projecting methyl.

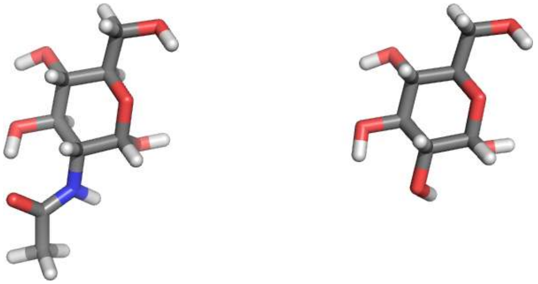

Figure 5.1: Stick models of α-D-Glc*p*NAc (*left*) and α-D-Glc*p* (*right*).

Previous studies have suggested that interresidual interactions involving *N*-acetyl groups influence the conformational behavior of hyaluronan.[102,103] Another study found that the amide bond in D-Glc*p*NAc exists in both the *cis* and *trans* forms, and that flexibility around the N–C2 bond is likely.[104]

For monosaccharides in solution the major conformation is *anti*, with the aliphatic hydrogen and the amide hydrogen pointing away from each other as depicted in Figure 5.1. In this conformation the torsion angle τ, defined by (O=)C–N–C2–C1, is close to 120°. For Glc*p*NAc residues in glycoprotein crystal structures this is the major conformation, while approximately 11% are in the *syn* conformation ($\tau \approx -60°$).[104]

During previous MD simulations we have observed a correlation between the conformation at the N–C2 bond and the conformation at a nearby glycosidic linkage in two different oligosaccharides; for the $\mathrm{Le^aLe^x}$ trisaccharide in Chapter 4 and for the pentasaccharide LNF-1.[63] In both cases, it was hypothesized that minor conformational states of the glycosidic torsion angles were available only for a certain conformation of the *N*-acetyl group.

This chapter describes the testing of this hypothesis by the use of MD simulations in which the *N*-acetyl torsion angle is locked in certain conformations.

5.2 The $\mathrm{Le^aLe^x}$ trisaccharide

For the trisaccharide discussed in the previous chapter (Figure 5.2), the non-*exo* conformation having negative values for the ϕ_4 torsion angle was present to 1% in the PARM22/SU01 simulation. One of the transitions to and from this conformation was studied in detail in Paper III revealing a series of events initiated by the rupture of the O5'···HO3 hydrogen bond, with the simultaneous formation of a hydrogen bond to the nearby *N*-acetyl carbonyl oxygen.

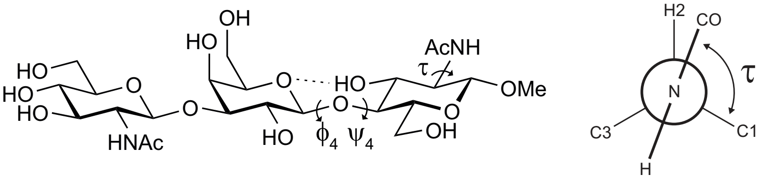

Figure 5.2: The $\mathrm{Le^aLe^x}$ trisaccharide studied in Chapter 4 with the discussed torsion angles indicated (*left*). Definition of τ (*right*).

Figure 5.3 shows the trajectories of the relevant torsion angles and hydrogen bonds during the series events discussed in Paper III. The transition to the non-*exo* conformation occurred through several metastable states, each associated with a specific hydrogen bonding pattern; a selection of these hydrogen bonds are shown in Figure 5.4. The non-*exo* conformation with $\phi_4 \approx -60°$ persisted for approximately 800 ps, stabilized by hydrogen bonding between O2' and O3. At the same time, ψ_4 was close to $-60°$; in contrast, ψ_4 fluctuated around 0° when ϕ_4 was in the *exo*-anomeric conformation.

Based on the hypothesis that the *exo*-anomeric conformation of ϕ_4 is destabilized when the *N*-acetyl carbonyl oxygen is suitably placed for accepting a hydrogen bond from HO3, additional MD simulations were

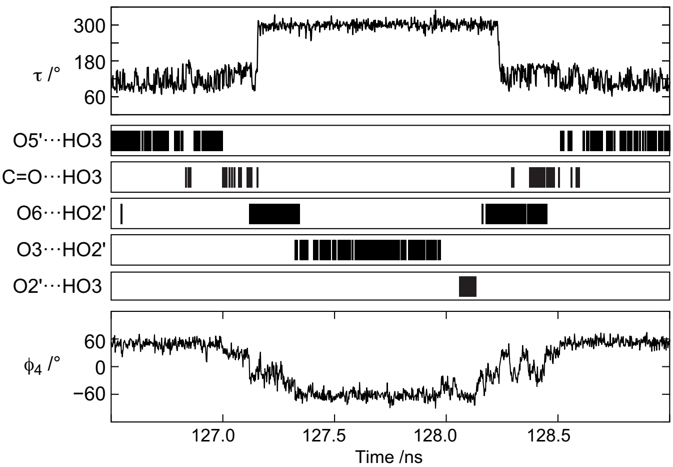

Figure 5.3: Time series for the part of the PARM22/SU01 MD simulation of the Le^{a}Le^{x} trisaccharide in which one of the transitions to the non-*exo* conformation occurs.

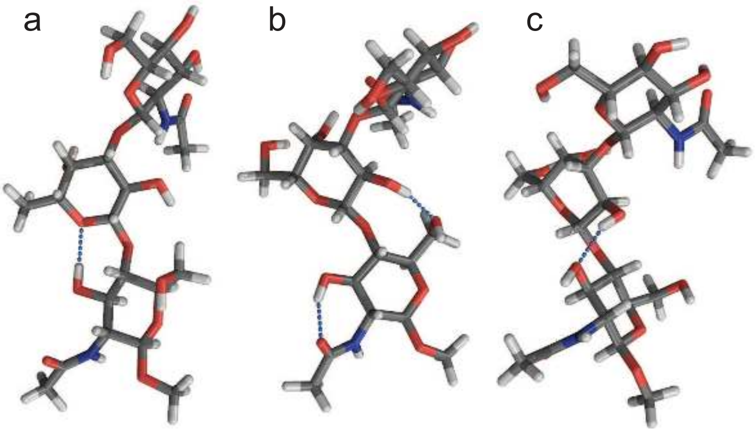

Figure 5.4: Molecular models of the trisaccharide highlighting hydrogen bonding at the β-D-Gal*p*-(1→4)-β-D-Glc*p*NAc linkage. (a) Hydrogen bonding between HO3 and O5' stabilizing the *exo*-anomeric conformation. (b) The *N*-acetyl oxygen competes for the HO3 donor, allowing a slight change in ϕ_4 so that HO2' can hydrogen bond to O6. (c) The non-*exo* conformation is stabilized by a hydrogen bond between HO2' and O3.

performed at 310 K. The probability distribution function for the τ torsion angle is shown in Figure 5.5a for the simulation without restraint. When τ is larger than 120° the *N*-acetyl carbonyl oxygen competes with O5' as the acceptor of hydrogen bonding from HO3. In order to evaluate the impact of the τ torsion angle on the conformational distribution at ϕ_4, two simulations were performed with τ restrained at $-60°$ (*syn*) and 165°, respectively.

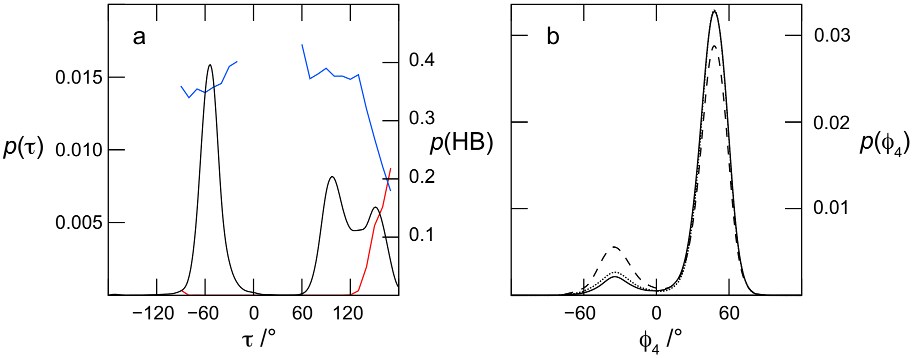

Figure 5.5: (a) PDF for the τ torsion angle in the unrestrained simulation and the probabilities of O5'$\cdots$HO3 (blue) and C=O$\cdots$HO3 (red) hydrogen bonding. (b) PDF for the ϕ_4 torsion angle in the same simulation (solid lines). Dots and dashed lines show the density as τ was kept at $-60°$ and 165°, respectively.

Probability distribution functions for the ϕ_4 torsion angle in the three simulations are shown in Figure 5.5b. The elevated temperature led to an increased amount of non-*exo* conformation; in the unconstrained simulation the population was 7% compared to 1% at 280 K. Restraining the τ to 165° led to an additional increase to 19% of the non-*exo* population at ϕ_4, whereas when τ was confined to $-60°$ the population (9%) was comparable to that in the unconstrained simulation.

A clear difference in hydrogen bonding was seen for the two constrained simulations; the O5'$\cdots$HO3 hydrogen bond was present during 34% of the $\tau = -60°$ simulation, compared to 25% in the $\tau = 165°$ simulation. This decrease is associated with an increase in the competing C=O$\cdots$HO3 hydrogen bonding, which was completely absent in the former simulation, but present to 13% in the latter. In conclusion, the *exo*-anomeric conformation at the ϕ_4 torsion angle is slightly destabilized when the *N*-acetyl carbonyl oxygen can compete with O5' for hydrogen bonding from HO3.

5.3 The *N*-acetyl group in LNF-1

The pentasaccharide lacto-*N*-fucopentaose (LNF-1) shown in Figure 5.6 was previously studied by our group using NMR spectroscopy and MD simulations. During an 18 ns MD simulation it was noted that the single visit to the non-*exo* conformation at the α-L-Fuc*p*-(1→2)-β-D-Gal*p* linkage coincided with the *N*-acetyl group being in the *syn* conformation ($\tau \approx -60°$), leading to the speculation that the *N*-acetyl group functioned as a conformational switch.[63] That the non-*exo* conformation is a minor conformation at the α-L-Fuc*p*-(1→2)-β-D-Gal*p* linkage is supported by an earlier study by Almond et al.[105]

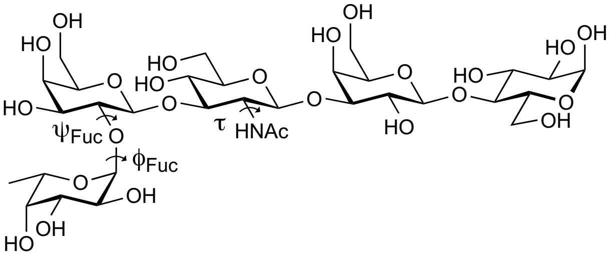

Figure 5.6: Schematic structure of LNF-1 with pertinent torsion angles indicated.

Three new MD simulations were performed, with the *N*-acetyl torsion angle restrained to +90° and −60°, and one in which it was not restrained. Figure 5.7 clearly demonstrates the increased population of the non-*exo* conformation at the α-(1→2) linkage when the *N*-acetyl torsion angle τ is −60°. The population of the non-*exo* conformation was 3% in the $\tau = +90°$ simulation and 28% in the simulation with $\tau = -60°$. Analysis of the ψ_{Fuc} torsion angle suggests that the two glycosidic linkages change in a concerted manner.

In contrast to the trisaccharide discussed above, transitions at the *N*-acetyl torsion angle were rare. For example, in the unrestrained 150 ns simulation the τ torsion was in the conformation with $\tau = -60°$ only two times, each time lasting several tens of nanoseconds. Notably, all motions at the glycosidic linkages in the simulation occur on a much shorter time scale.

Because of the slow dynamics at the *N*-acetyl torsion, the correlation between the τ torsion angle and increased flexibility at the α-(1→2) linkage is apparent also in the unrestrained simulation (cf. Figure 5 in Paper IV).

The causal link between the *N*-acetyl conformation and the α-(1→2) non-*exo* conformation is likely a combination of steric effects and hydrogen

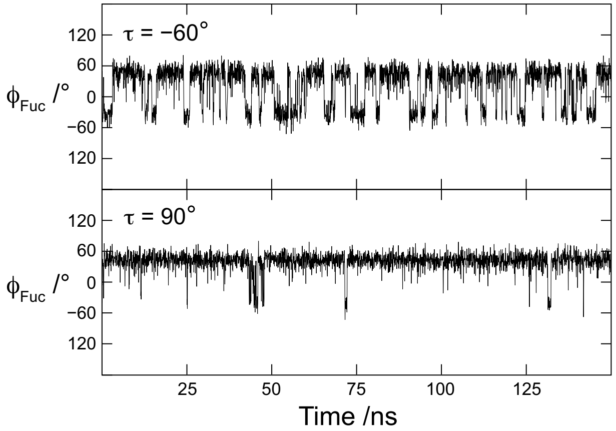

Figure 5.7: Time series for the ϕ_{Fuc} torsion angle in LNF-1 in the two MD simulations where τ was restrained as indicated.

bonding as depicted in Figure 5.8. In the non-*exo* conformation at ϕ_{Fuc}, a hydrogen bond between the *N*-acetyl NH and O5 in the fucose residue can be formed when the *N*-acetyl torsion angle is close to $-60°$. In the simulation with $\tau = -60°$, the $\mathrm{O5_{Fuc}} \cdots \mathrm{HN}$ hydrogen bond was present to 45% in the non-*exo* conformation.

Rotation of the *N*-acetyl to the other observed conformation ($\tau = 90°$) would bring the methyl groups of the *N*-acetyl and the fucose uncomfortably close to each other. The combination of this *N*-acetyl conformation with the non-*exo* conformation is thereby disfavored.

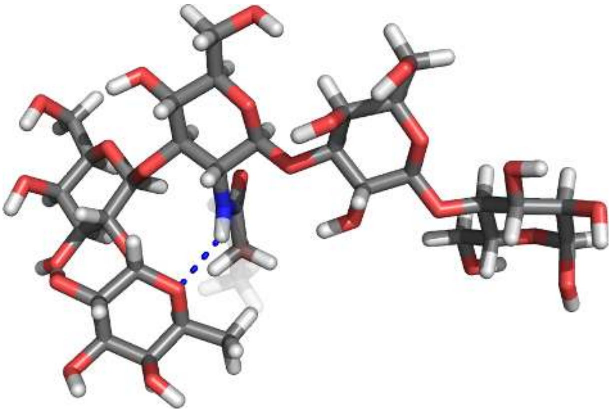

Figure 5.8: Molecular model for LNF-1 having the non-*exo* conformation at the α-L-Fuc*p*-(1→2)-β-D-Gal*p* linkage, stabilized by the hydrogen bond that is possible when $\tau = -60°$ (blue dashes). The semi-transparent *N*-acetyl group has $\tau = 90°$.

The conformation with $\tau = -60°$ is likely not significantly populated for LNF-1 in aqueous solution,[106] and hence the α-L-Fuc*p*-(1→2)-β-D-Gal*p* linkage is conformationally restricted by the *N*-acetyl group, as has been suggested previously.[105]

5.4 Conclusions

For two oligosaccharides, the conformation of an *N*-acetyl group was shown to influence the conformation at a nearby glycosidic linkage.

In the case of the $\text{Le}^{\text{a}}\text{Le}^{\text{x}}$ trisaccharide this is achieved in a certain *N*-acetyl conformation by competing with the $\text{O5}' \cdots \text{HO3}$ hydrogen bond that stabilizes the *exo*-anomeric conformation.

For LNF-1, the secondary, non-*exo* conformation of the α-L-Fuc*p*-(1→2)-β-D-Gal*p* linkage is incompatible with one of the two *N*-acetyl conformations for steric reasons. In the other conformation of the *N*-acetyl group, the non-*exo* conformation is stabilized by a hydrogen bond from the amide hydrogen. Although the *N*-acetyl conformation with $\tau = -60°$ is likely populated to a minor extent, the results from the MD simulation without restraints to this torsion angle highlight the importance of monitoring the *N*-acetyl conformation during MD simulations. Since dynamics at this torsion angle are much slower than at any of the glycosidic linkages, a simulation might appear to be converged when in fact it is not; the same argument applies to other degrees of freedom with slower dynamics than for the monitored degrees of freedom.

6. Conformation and Dynamics of β-L-Fuc$p$-(1→6)-α-D-Glc$p$-OMe (Paper V)

6.1 Background

Among the possible pyranose disaccharides, the (1→6)-linked ones present the greatest challenge to the investigator of conformational preferences. This is due to the fact that the orientation of the two monosaccharide residues are determined by the rotation around three bonds. Previous studies on carbohydrates bearing an equatorial hydroxyl group at C4 (as in e.g. glucose) have concluded that in an aqueous environment, glycosylation at O6 does not have a large impact on the conformational equilibrium at the ω torsion angle. The ϕ torsion angle prefers the conformation stabilized by the *exo*-anomeric effect, and for the ψ torsion angle, repulsive steric interactions are minimized at values close to 180°. The latter torsion angle is expected to have a rather large conformational freedom, either as a broad distribution or with some population of states at either +90° or −90°.[18,74,107–110]

This chapter and the next concern the conformation of (1→6)-linked disaccharides. In the present study, the conformation and dynamics of β-L-Fuc$p$-(1→6)-α-D-Glc$p$-OMe (Figure 6.1) were investigated using a combined approach of MD simulation and NMR spectroscopy.

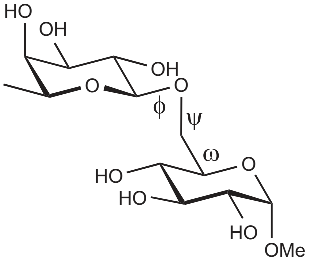

Figure 6.1: Schematic representation of β-L-Fuc$p$-(1→6)-α-D-Glc$p$-OMe (**F6G**).

6.2 Conformation

6.2.1 MD simulation

The conformational equilibrium obtained from a 500 ns MD simulation using the PARM22/SU01 force field[54] agrees well with the qualitative description found in previous publications and outlined above. Both the ω and ψ torsion angles showed frequent conformational transitions, in contrast to the ϕ torsion angle which was exclusively in the *exo*-anomeric conformation. For the ω torsion angle, the *gt* ($\omega \approx +60°$) and *gg* ($-60°$) conformers were present to 72% and 27%, respectively. At the ψ torsion angle, the *antiperiplanar* ($\psi \approx 180°$) conformer and a *clinal* (85°) conformer were present in a 95:5 ratio. The accessible conformational space for these two torsion angles is shown in the two-dimensional potential of mean force (Figure 6.2).

The only interresidual hydrogen bond occurred between O5*g* and HO2*f* (Figure 6.2). This was present to 8% and 11% in the *clinal*/*gt* and *clinal*/*gg* conformations, respectively, but was absent in the other conformations.

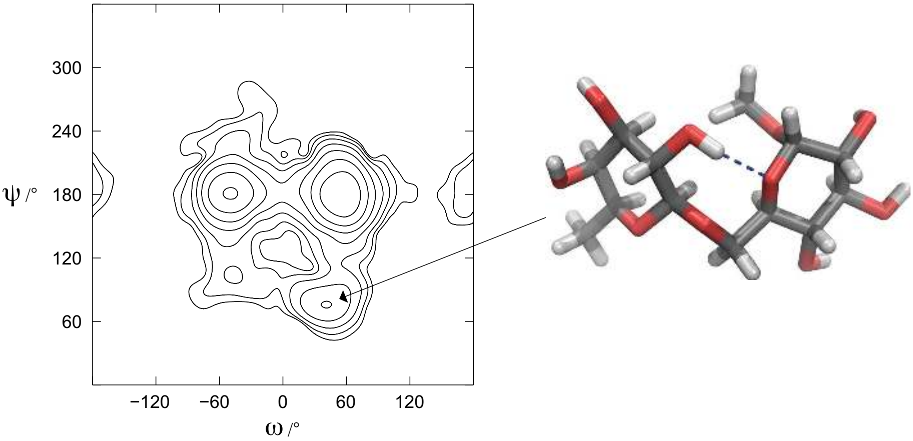

Figure 6.2: Two-dimensional potential of mean force as a function of the ψ and ω torsion angles in steps of $k_\mathrm{B}T$ up to $7 \times k_\mathrm{B}T$ (*left*). The *clinal*/*gt* conformation with $\mathrm{O5}g\cdots\mathrm{HO2}f$ hydrogen bonding (*right*).

6.2.2 Refinement using NMR parameters

NMR parameters sensitive to the conformational preferences at the glycosidic linkage were measured, and the determined values are presented in Tables 6.1 and 6.2.

In the ^{1}H,^{1}H–NOESY spectrum obtained with excitation of H1*f*, an interesting observation is the magnetization transfer to H5*g* shown in Figure 6.3. Due to the overlap with H5*f*, the cross-relaxation rate was determined using the STEP-NOESY experiment.[111] Magnetization was transferred from H2*g* to H5*g* via isotropic mixing prior to inversion of H5*g*, and subsequently the cross-relaxation to H1*f* could be measured (cf. Figures 4 and 5 in Paper V).

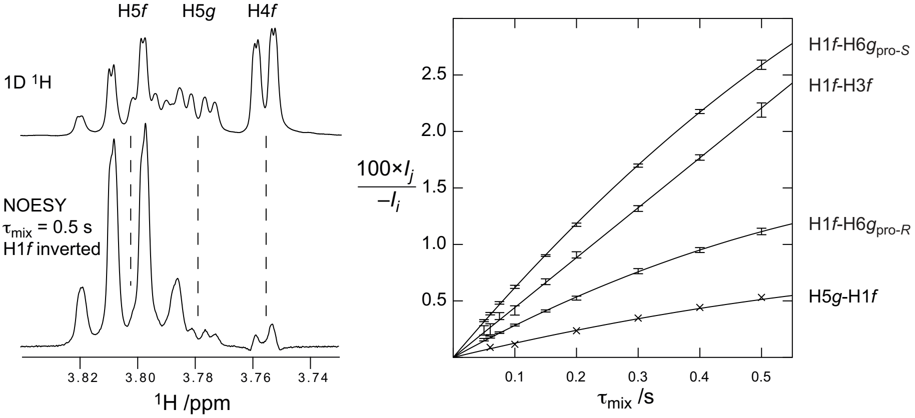

Figure 6.3: Selected region of proton and NOESY spectra showing magnetization transfer to H5*g* after inversion of H1*f*, partially obscured by overlap with the H5*f* resonance (*left*). Normalized buildup of magnetization due to cross-relaxation with H1*f* (*right*). Error bars correspond to the standard deviations for experimental points while lines are fitted functions; crosses are averages from two experiments.

The determined distance between H1*f* and H5*g*, 3.18 Å, indicates deviations from the *antiperiplanar* conformation of the ψ torsion angle. When $\psi \approx 180°$, this distance is longer than 4 Å regardless of ϕ and ω.

The agreement between predicted and measured parameters was quantified using the χ^2 value. Calculating the parameters directly from the MD simulation yielded a fairly large error ($\chi^2 = 52$). A large fraction of this error, 68%, comes from the coupling constants related to the ω torsion angle, especially the $^3J_{\mathrm{H5,H6}R}$ coupling constant. The value of the latter was determined to be 4.9 Hz from experiment, while the MD simulation gave a value of 7.6 Hz. This discrepancy could come either from an incorrect ratio of the *gt* and *gg* conformations, from a slightly incorrect geometry in these conformations, or both.

Errors in populations are likely since a small error in energy difference between two states of similar energy will result in a large error in their populations (cf. Figure 1.8). However, the calculated values for $^3J_{\mathrm{H5,H6}S}$

Table 6.1: Scalar coupling constants (Hz) determined by NMR spectroscopy, from MD simulation, and from population fitting.

Torsion	$^{2/3}J$	NMR	MD	Fitting 6 states[a]	Fitting 4 states[b]
ω	H5g,H6$g_{\text{pro}-R}$	4.89	7.55	5.19	5.23
ω	H5g,H6$g_{\text{pro}-S}$	2.15	3.35	2.19	1.82
ω,ψ	H6$g_{\text{pro}-R}$,H6$g_{\text{pro}-S}$	−11.7	−9.0	−10.4	−10.3
ω	C4g,H6$g_{\text{pro}-R}$	1.26	3.36	1.88	1.66
ω	C4g,H6$g_{\text{pro}-S}$	3.20	4.93	3.81	3.84
ψ	C1f,H6$g_{\text{pro}-R}$	3.23	2.18	3.20	3.07
ψ	C1f,H6$g_{\text{pro}-S}$	3.03	1.83	2.59	2.52
ϕ	C6g,H1f	4.39	3.27	–[c]	–
		χ^2	41.1	2.2	2.5

[a] Combinations of 2 states for ψ and 3 states for ω.

[b] Combinations of 2 states for ψ and 2 states for ω.

[c] Not used in population fitting nor in calculations of χ^2.

Table 6.2: Effective distances (Å) determined by NMR spectroscopy, from MD simulation, and from population fitting.

Torsion	Proton pair	NMR NOE	NMR T-ROE	MD	Fitting 6 states[a]	Fitting 4 states[b]
ϕ,ψ	H1f–H6$g_{\text{pro}-R}$	2.77	2.78	2.80	2.89	2.88
ϕ,ψ	H1f–H6$g_{\text{pro}-S}$	2.41	2.45	2.40	2.43	2.43
ϕ,ψ,ω	H1f–H5g	3.18	–[c]	3.72	3.17	3.12
ω	H4g–H6$g_{\text{pro}-R}$	2.72	2.76	2.53	2.74	2.72
ω	H4g–H6$g_{\text{pro}-S}$	3.02	3.03	3.17	3.11	3.17
			χ^2	10.9	1.1	1.5

[a] Combinations of 2 states for ψ and 3 states for ω.

[b] Combinations of 2 states for ψ and 2 states for ω.

[c] Not determined.

in the individual conformations at the ω torsion angle were at least 1 Hz larger than the experimental value. This was also the case for the $^3J_{\mathrm{C4,H6}R}$ coupling constant. Clearly, these states cannot be combined to explain the observed coupling constants.

The average torsion angle for ω in the *gt* and *gg* conformers was +53° and −47° respectively; in contrast, values of ω are often found to be close to +65° for *gt* and −65° for *gg* in geometries determined by X-ray crystallography.[13,112] As has previously been reported, interpreting the $^3J_{\mathrm{H5,H6}R/S}$ coupling constants in **F6G** as a three-state equilibrium gives the relative populations 42:50:8 for the *gt*:*gg*:*tg* conformers, respectively, when using $|\omega| = 65°$ for the *gauche* conformers.[36]

For the ϕ torsion angle, a single conformation with $\phi = -40°$ is sufficient to rationalize the heteronuclear three-bond coupling constant, while the heteronuclear coupling constants related to ψ cannot be satisfied by a single, reasonably narrow conformation.

A population fitting was performed, using the conformations outlined above, viz. $\phi = -40°$, $\psi = 180°/85°$, and $\omega = +65°/-65°$. The χ^2 value was minimized by adjusting the populations of these states. This gave a 49:51 ratio between the *gt*:*gg* conformations and a 71:29 ratio between the *antiperiplanar*:*clinal* conformations. The calculated parameters were in good agreement with values from NMR spectroscopy as shown in Tables 6.1 and 6.2 (4 states, $\chi^2 = 4.0$). The error was not reduced significantly when the *gt*:*gg* ratio was optimized individually for the two conformations of ψ ($\chi^2 = 3.9$). Neither the inclusion of the *tg* conformation (6 states, $\chi^2 = 3.3$), nor a smaller ω torsion angle in the *gt*/*clinal* conformation (cf. Figure 6.2) gave a significant improvement in the χ^2 value.

6.3 Interactions with water from MD

By means of spatial distribution functions,[113] high-density regions of water around the molecule were visualized for the two major conformations (Figure 6.4). The regions of highest density all occurred in proximity to the glycosidic linkage. This is likely due to a favorable arrangement of the oxygen atoms in the cavity formed between the two pyranose rings. This allows water molecules to participate in hydrogen bonding with two or more oxygen atoms or hydroxyl hydrogen atoms.

It might be tempting to assume that such water molecules are tightly bound when interacting with this region. However, the average residence time for water molecules interacting with the acetal oxygens (10 ps) was qualitatively similar to water molecules interacting with the hydroxyl groups (8 ps) in the molecule. Thus, in all cases water molecules are rapidly exchanged.

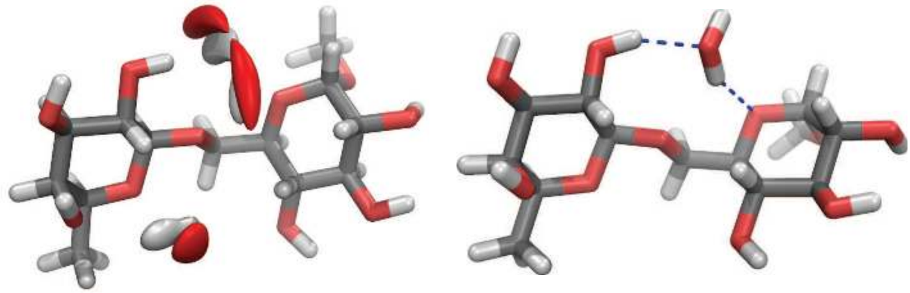

Figure 6.4: Spatial distribution function calculated for the *antiperiplanar/gg* conformation (*left*). High density regions of water are enclosed in red and white surfaces for oxygen and hydrogen, respectively. Snapshot from the MD simulation showing a water-bridged hydrogen bond (*right*).

6.4 Dynamics

6.4.1 Dynamics from NMR spectroscopy

The motional properties of the disaccharide were studied using three different approaches; the translational diffusion using pulsed field gradient experiments, the ratio of NOESY and T-ROESY cross-relaxation rates, and ^{13}C T_1 relaxation times. The two latter parameters obtain their motional sensitivity from the spectral density functions and hence report on correlation times. Via the Stokes-Einstein (Equation 6.1) and Debye-Stokes (Equation 6.2) relationships, the translational diffusion constant can be calculated from the correlation time and vice versa.[114]

$$D_{\mathrm{t}} = \frac{k_{\mathrm{B}}T}{6\pi\eta r_{\mathrm{h}}} \tag{6.1}$$

$$\tau_{\mathrm{c}}^{\mathrm{iso}} = (6D_{\mathrm{r}})^{-1} = \frac{8\pi\eta r_{\mathrm{h}}^3}{6k_{\mathrm{B}}T} \tag{6.2}$$

Here the shape is assumed to be spherical, η is the viscosity, and r_{h} is the hydrodynamic radius. The translational diffusion constant, 4.61×10^{-10} m$^2 \cdot$ s^{-1}, was used to calculate the isotropic correlation time $\tau_{\mathrm{c}}^{\mathrm{iso}}$, yielding 116 ps. This is in excellent agreement with individual effective correlation times, τ_c^{eff}, obtained for the various ^{1}H-^{1}H interaction vectors (117–123 ps).

For the ^{13}C T_1 relaxation times (Figure 6.5), a striking feature is the fast relaxation of C4*f* compared to all other carbon atoms in the molecule. In contrast, the other carbon atoms in the fucose moiety experience slower and remarkably similar relaxation times. This prompted us to investigate the possibility of anisotropic rotational diffusion, as the molecule has a rather prolate shape, being longest approximately in the direction of the C4*f*-H4*f* vector (Figure 6.6). Thus, this vector is less sensitive to the faster rotation around the long axis ($D_{\|}$) than around the perpendicular axes ($D_{\perp}$).

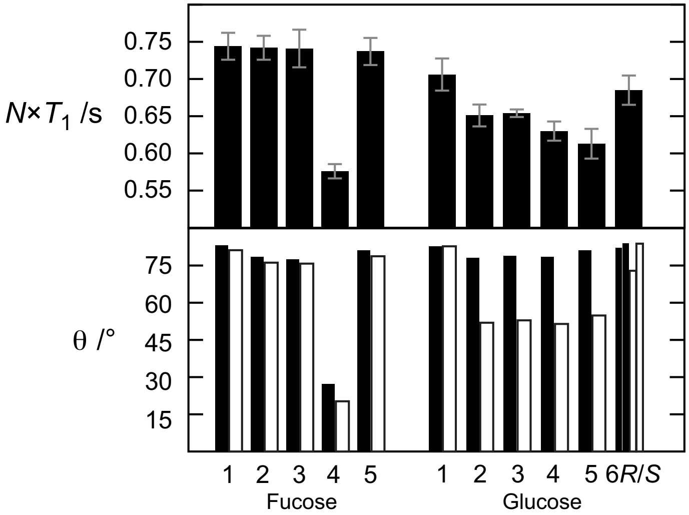

Figure 6.5: Experimentally determined ^{13}C T_1 relaxation times (*top*) and angles between the corresponding CH bond vectors and the unique axis of the moment of inertia tensor from the MD simulation (*bottom*) for the *gt* (filled bars) and *gg* (empty bars). N is the number of bound protons.

Anisotropy has previously been used to rationalize the faster relaxation of C4$_{\mathrm{Gal}}$ in lactose (β-D-Gal*p*-(1→4)-D-Glc*p*) and in methyl β-lactoside, compared to the other carbon atoms in these compounds.[115,116] Both lactose and **F6G** share the feature of an axial hydroxyl substituent at position 4 in the terminal residue, and consequently the hydrogen atom in this position is equatorially oriented.

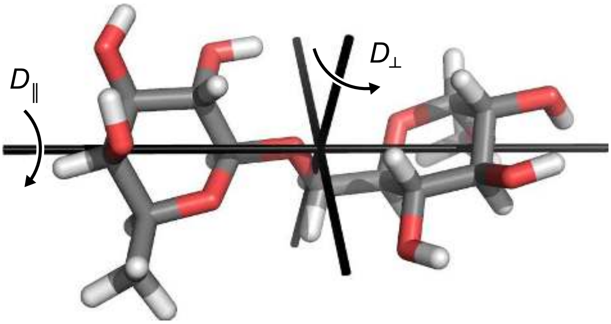

Figure 6.6: Molecular model with idealized torsion angles for the *antiperiplanar/gg* conformation; $\phi = -40°$, $\psi = 180°$, and $\omega = -65°$. The axes of the moment of inertia tensor, and the rotational motions associated with $D_{\parallel}$ and $D_{\perp}$ are shown.

6.4.2 Dynamics from MD simulations

From MD simulations, the translational diffusion constant was determined to be 4.95×10^{-10} $\mathrm{m}^2 \cdot \mathrm{s}^{-1}$, which is in good agreement with the experimentally determined value, and corresponds to a correlation time, $\tau_{\mathrm{c}}^{\mathrm{iso}}$, equal to 95 ps.

Rotational diffusion was addressed using P_2 correlation functions[i] for a set of atom-atom vectors with different orientations (Figure 6.7), and for the unique axis of the moment of inertia tensor. Assuming axial symmetry, the diffusion tensor was fitted for the *antiperiplanar gt* and *gg* conformations. In both cases, the angle between the main axis of the fitted diffusion tensor and of the inertia tensor was less than 8°. The determined rotational diffusion constants correspond to an average isotropic correlation time equal to 95 ps and ${}^{D_{\parallel}}/_{D_{\perp}} = 2.35$.

It is evident that the anisotropy is responsible for a large part of the differences in observed relaxation times, with a good correlation with the orientations of the CH vectors (Figure 6.5), especially in the *gg* conformation. Generalized order parameters, S^2, were determined from P_2 correlation functions after removing overall molecular motion. These were used together with the fitted rotational diffusion constants to calculate ^{13}C T_1 relaxation times for the conformational distribution obtained above. For this calculation, the axes of the diffusion tensor and inertia tensor were approximated to coincide.

---

[i] Defined as $C_2(t) = \langle P_2\left[\boldsymbol{\mu}(0) \cdot \boldsymbol{\mu}(t)\right]\rangle$ where $P_2(x) = (3\cos^2(x) - 1)/2$.

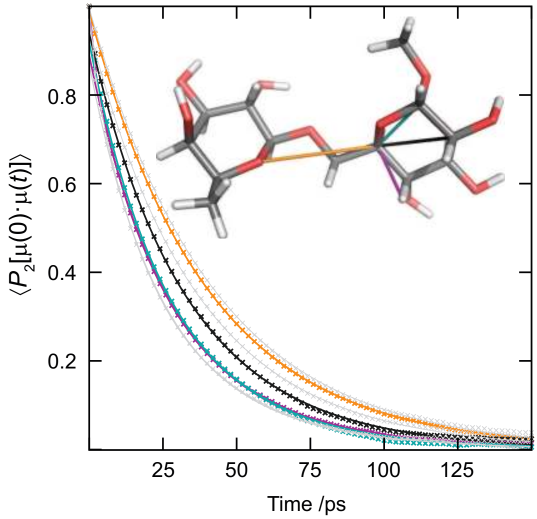

Figure 6.7: Laboratory frame P_2 correlation functions for the *antiperiplanar/gt* conformation from MD simulation (×) and from fitting (lines) of the diffusion tensor. Gray lines correspond to vectors not shown in the model.

The calculated ^{13}C T_1 relaxation times are in good agreement with the experimentally determined values (cf. Figure 11c in Paper V). Since the observed relaxation times can be rationalized without accounting for fast conformational transitions at the glycosidic linkage, such transitions are likely slow compared to the overall rotation. From the MD simulation, the conformational transitions at the ψ and ω torsion angles were found to be slightly slower than overall rotation.

Since anisotropy can be expected to influence the spectral density function at frequencies involved in NOESY and T-ROESY measurements, cross-relaxation rates were calculated as a function of the orientation of an interacting ^{1}H-^{1}H vector. As seen in Figure 6.8, the two experiments are differently sensitive to anisotropy in this case, with T-ROESY being affected the most. In the worst case, the two vectors connecting the reference interaction and the unknown interaction have orientations corresponding to the maximum and the minimum cross-relaxation rates, respectively, or vice versa. The maximum difference in cross-relaxation rate due to anisotropy is 6% for the NOE. For the T-ROE this value is 28% (Figure 6.8), making the latter experiment more sensitive to anisotropy than the former. The effect is smaller for the derived effective distances, namely 1% for the NOE and 4.2% for the T-ROE. Hence, this source of error was neglected in the conformational analysis.

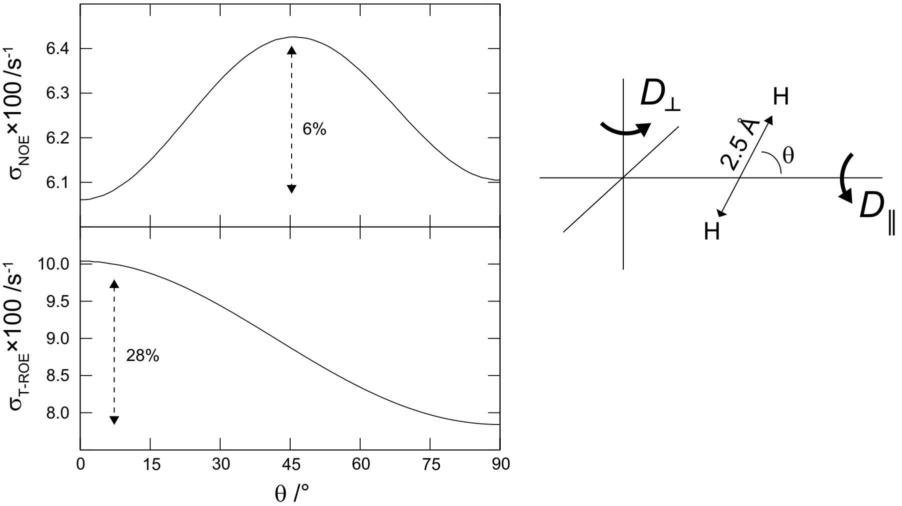

Figure 6.8: Cross-relaxation rates calculated as a function of the angle between the ^{1}H,^{1}H interaction vector and the unique axis of the diffusion tensor. Calculated using the rotational diffusion constants obtained from the MD simulation and assuming a distance of 2.5 Å, $S^2 = 1$ and $\nu_H = 600.15$ MHz.

The different susceptibility towards anisotropic diffusion for the different types of cross-relaxation rates only occurs in the region of intermediate motion.[117] In this particular case the error from neglecting anisotropy is smaller for both NOE and T-ROE than it would be in the fast or slow motion limits. However, at other intermediate correlation times the error would be larger. Close to the NOE zero-crossing, the T-ROESY experiment performs better.

6.5 Conclusions

For β-L-Fuc*p*-(1→6)-α-D-Glc*p*-OMe, the conformational and dynamical properties have been elucidated using a combination of MD simulation and NMR spectroscopy. The conformational ensemble predicted by the MD simulation was adjusted using data from NMR spectroscopy. Four major conformational states are populated, viz. the combinations of the *gt*/*gg* conformations at ω and the *antiperiplanar* and *clinal* conformations at ψ. A considerable population of the *clinal* conformation at ψ was found, with the strongest experimental evidence being the short distance between H1*f* and H5*g* (3.18 Å). This can only be explained by the presence of conformational states other than the *antiperiplanar*. Additionally, it was found that the magnitude of the ω torsion angle is underestimated in the *gt* and *gg* conformations. These are more adequately described by a magnitude equal to ±65°.

As has been pointed out previously,[115,116,118] it is important to consider effects of anisotropic diffusion before inferences are made about internal motions in oligosaccharides. The ^{13}C T_1 relaxation times measured for **F6G** were shown to be adequately explained by anisotropy. Hence, the conformational transitions occur slower than overall rotation.

The impact of anisotropy on effective distances calculated using the ISPA was shown to be small for this case, with the error being less for the NOE than for the T-ROE. However, at other correlation times the opposite is true. It is therefore advisable to choose the method for cross-relaxation measurements with care in the region of intermediate motion.

7. Conformations of (1→6)-Linked Di- and Trisaccharides (Paper VI)

7.1 Background

As pointed out in Chapter 6, the conformational analysis of (1→6)-linked oligosaccharides is particularly challenging. It is desirable to understand the influences of the identity of the two component monosaccharides on the conformational equilibrium. To enable the understanding of such influences, force fields need to be refined to the point where conformational trends are predicted accurately and where experimentally determined parameters are reproduced within error limits.

In the present study, the CHARMM36 carbohydrate force field[119] parameters for the ω torsion angle in (1→6)-linkages were reoptimized in order to better reproduce available experimental data.

Due to the scarcity of available experimental data, nine (1→6)-linked disaccharides and one trisaccharide containing a (2→6)-linkage, shown in Figure 7.1, were investigated using NMR spectroscopy in order to determine conformationally sensitive homo- and heteronuclear J-coupling constants for all compounds. Additionally, nuclear Overhauser effects were measured for two of the compounds.

7.2 NMR spectroscopy

7.2.1 Coupling constants

Homonuclear $^1H,^1H$ coupling constants (Table 7.1) were determined using the PERCH software,[39] by iteratively adjusting the chemical shifts and coupling constants until the spin-simulated spectra agreed with the experimental spectra, as demonstrated in Figure 7.2 for compound **3**. For compound **3**, two site-specifically labeled isotopologues were available. Therby, also heteronuclear coupling constants could be determined by spin-simulation. Of special interest for the conformational analysis of (1→6)-linked oligosaccharides are the coupling constants between H5 and $H6_{\mathrm{pro}-R/S}$ which are sensitive to the ω torsion angle, as well as the geminal $^2J_{H6R,H6S}$ coupling constant which reports on both ω and ψ.[36]

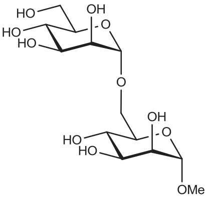
HO
OH
HO
HO
O
O
OH
HO
HO
O
OMe

α-D-Man*p*-(1→6)-α-D-Man*p*-OMe (**1**)

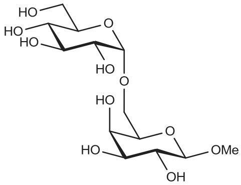
HO
HO
HO
O
HO
O
HO
O
HO
OMe
OH

α-D-Glc*p*-(1→6)-β-D-Gal*p*-OMe (**6**)

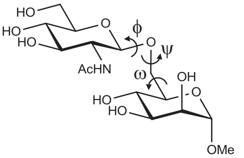
HO
HO
HO
O
AcHN
ϕ
O
ψ
ω
OH
HO
HO
O
OMe

β-D-Glc*p*NAc-(1→6)-α-D-Man*p*-OMe (**2**)

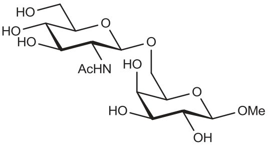
HO
HO
HO
O
O
AcHN
HO
O
HO
OMe
OH

β-D-Glc*p*NAc-(1→6)-β-D-Gal*p*-OMe (**7**)

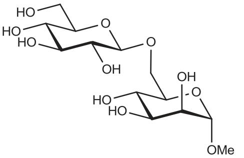
HO
HO
HO
O
O
OH
OH
HO
HO
O
OMe

β-D-Glc*p*-(1→6)-α-D-Man*p*-OMe (**3**)

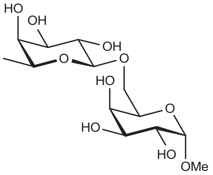
HO
OH
OH
O
O
HO
O
HO
HO
OMe

β-L-Fuc*p*-(1→6)-α-D-Gal*p*-OMe (**8**)

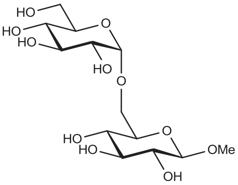
HO
HO
HO
O
HO
O
HO
HO
O
OMe
OH

α-D-Glc*p*-(1→6)-β-D-Glc*p*-OMe (**4**)

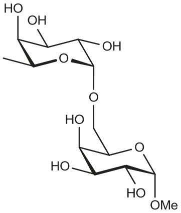
HO
OH
OH
O
O
HO
O
HO
HO
OMe

α-L-Fuc*p*-(1→6)-α-D-Gal*p*-OMe (**9**)

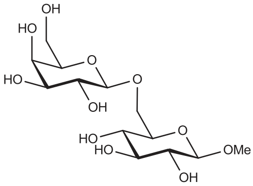
OH
HO
O
HO
O
OH
HO
HO
O
OMe
OH

β-D-Gal*p*-(1→6)-β-D-Glc*p*-OMe (**5**)

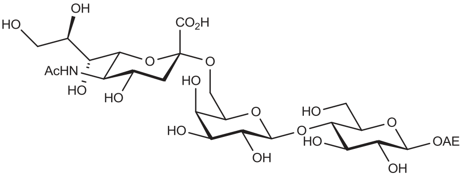
HO
OH
CO_2H
O
O
AcHN
HO
HO
HO
O
HO
O
HO
O
HO
OAE
OH
OH

α-Neu5Ac-(1→6)-β-D-Gal*p*-(1→4)-β-D-Glc*p*-OAE (**10**)

Figure 7.1: Disaccharides (and one trisaccharide) used in this study. Compounds **1**–**5** have an equatorial hydroxyl group at C4 (*gluco*-configuration) in the reducing end residue. Compounds **6**–**10** have an axial hydroxyl group at this position (*galacto*-configuration).

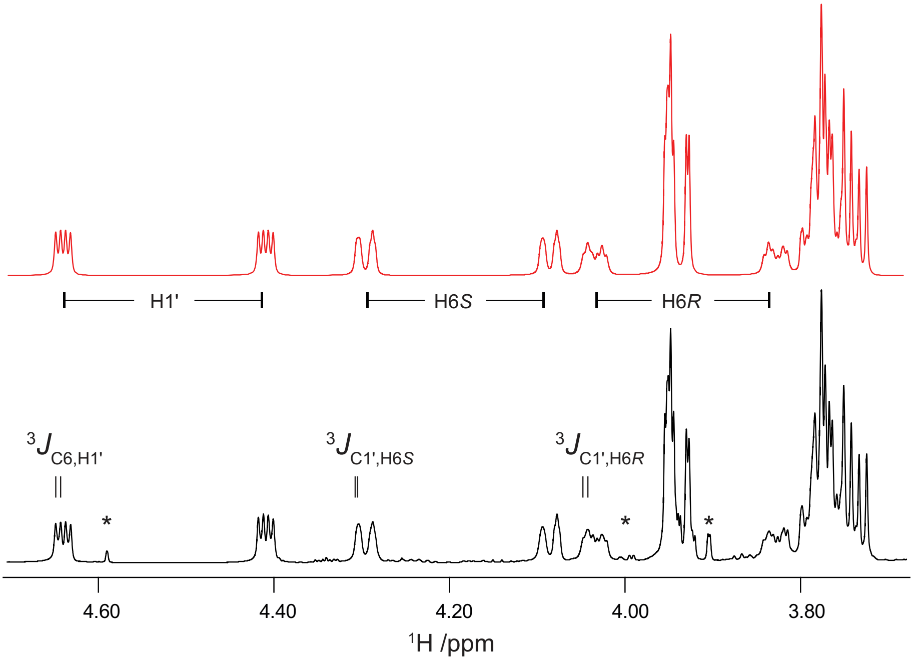

Figure 7.2: Selected region of experimental (*bottom*) and simulated (*top*) ^{1}H spectra for the site-specifically labeled compound [1',6–$^{13}C_2$]-**3**. Asterisks indicate impurities.

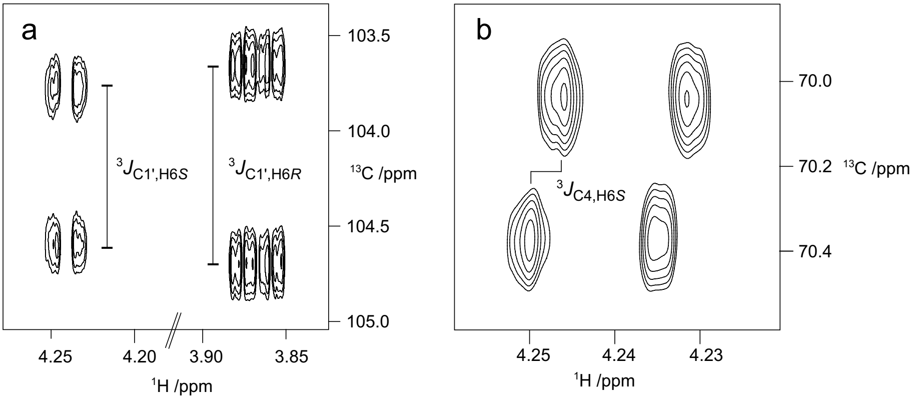

Figure 7.3: Selected region of J-HMBC (a) and HSQC-HECADE (b) spectra for compound **5**.

Homonuclear ^{1}H,^{1}H coupling constants are typically not observed across the glycosidic linkage oxygen. However, heteronuclear ^{13}C,^{1}H coupling constants are a valuable source of information pertaining to the $\phi_{\mathrm{O5'}}$ and ψ torsion angles, namely the $^{3}J_{\mathrm{C6,H1'}}$ and $^{3}J_{\mathrm{C1',H6}R/\mathrm{S}}$ coupling constants, respectively.

Heteronuclear ^{13}C,^{1}H coupling constants were determined using the J-HMBC[42] and HSQC-HECADE[43] experiments. The determined values are presented in Table 7.4. Examples of these spectra are shown for compound **5** in Figure 7.3. From these experiments it was also possible to determine values for ^{13}C,^{1}H coupling constants reporting on the ω torsion angle, viz. $^{3}J_{\mathrm{C4,H6}R/S}$ and $^{2}J_{\mathrm{C6,H5}}$, for some of the compounds (Tables S1 in Paper VI).

7.2.2 Nuclear Overhauser effects

For two of the compounds, viz. α-D-Glc*p*-(1→6)-β-D-Gal*p*-OMe (**6**) and β-L-Fuc*p*-(1→6)-α-D-Gal*p*-OMe (**8**), NOESY experiments were used to determine cross-relaxation rates and thus effective distances across the glycosidic linkage. For compound **8** an example of a NOESY spectrum is given in Figure 7.4 and the extents of magnetization transfer at different mixing times are shown in Figure 7.5. Effective distances are given in Table 7.3 together with the corresponding values determined from MD simulations.

For both molecules, the H6$_{\mathrm{pro-}R}$ resonance was obscured by overlapping resonances when excitation was performed at H1' so that only the sum of cross-relaxation rates could be determined. For the H6$_{\mathrm{pro-}S}$ resonance in **6**, there was overlap with the H3' and H5' resonances. However, since these distances are relatively independent of conformation, their estimated contributions to the combined cross-relaxation rates were removed, as has been described[120,121] and validated[73] in previous publications from the Widmalm group.

7.3 Force field verification

Hamiltionan replica exchange[122] MD simulations were used to determine the conformational equilibria for compounds **1**–**10** with the improved set of parameters. Two-dimensional PMFs are shown in Figures 3 and 4 in Paper VI.

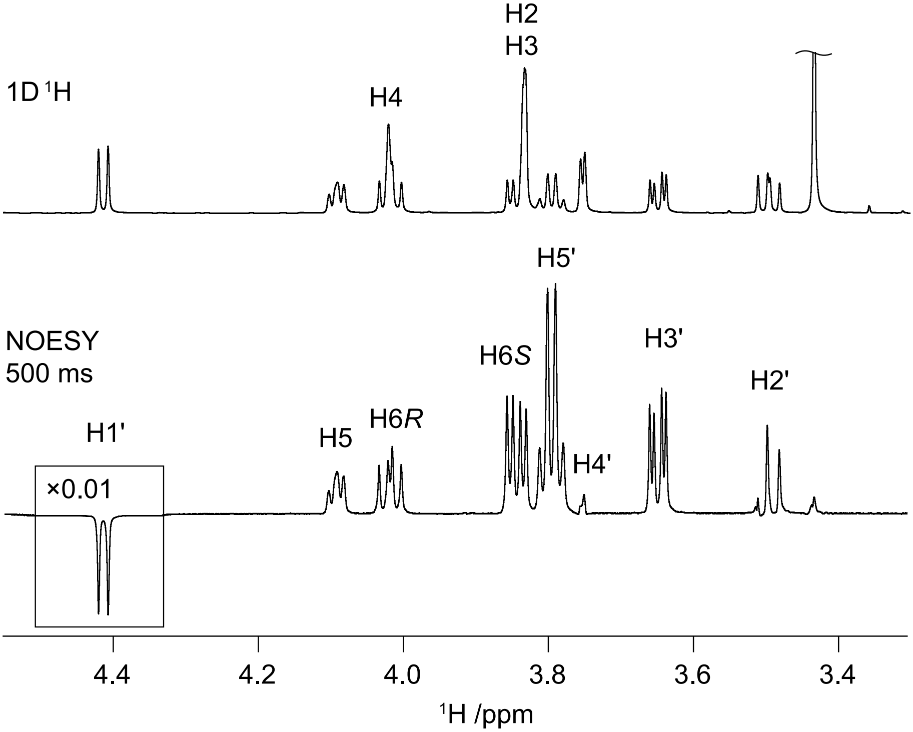

Figure 7.4: 1D ^{1}H (*top*) and NOESY (*bottom*) spectra for compound **8**. Note that there is possibly a small contribution from H4 in the peak labeled as H6*R*.

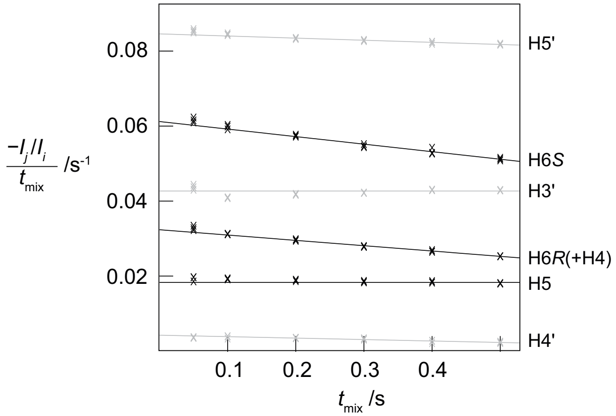

Figure 7.5: Normalized peak integrals divided by mixing time versus mixing time for NOESY experiments with inversion of H1' in compound **8**. Lines were fitted to the experimental values shown by crosses.

7.3.1 The ω torsion angle

The previous form of the force field was found to be biased, favoring the *gg* conformation for the ω torsion angle regardless of the stereochemistry at position 4 in the reducing end residue. This trend is reflected in the too small predicted values for $^3J_{\mathrm{H5,H6}R}$, which were in the range 0.7–2.0 Hz (cf. Table S2 in Paper VI). Experimentally, these values are around 4—6 Hz for compounds **1**–**5** which have an equatorial hydroxyl group at C4, and around 7—8 Hz for the other compounds, in which the corresponding hydroxyl group is axially oriented (Table 7.1).

Table 7.1: Homonuclear ^{1}H,^{1}H coupling constants in Hz related to the ω torsion angle.

	$^3J_{\mathrm{H5,H6}R}$		$^3J_{\mathrm{H5,H6}S}$		$^2J_{\mathrm{H6}R,\mathrm{H6}S}$[a]	
Compound	NMR	MD	NMR	MD	NMR	MD
1	5.1	5.1	2.0	2.8	−11.3	−9.8
2	6.5	6.1	1.9	1.8	−11.3	−9.6
3	5.4	5.4	2.0	1.8	−11.5	−9.4
4	4.3	4.2	2.1	2.8	−11.1	−9.4
5	5.6	6.1	2.1	1.8	−11.7	−9.5
6	7.2	7.0	5.1	4.0	−10.6	−9.4
7	7.8	7.7	4.1	3.5	−10.7	−9.4
8	7.4	6.3	5.0	4.5	−11.0	−9.6
9	7.7	7.7	4.6	4.5	−10.7	−9.2
10	8.4	7.8	3.9	4.3	−10.4	−9.0

[a] Also sensitive to the ψ torsion angle.

The new parametrization for the ω torsion was derived using larger model compounds than the previous parametrization. The moiety linked to O6 was extended from a methyl group to a tetrahydropyranyl group. This led to a significant improvement in the conformational distribution for the ω torsion angle, as confirmed by the improved agreement with experimentally determined coupling constants related to this torsion angle (Table 7.1).

Populations of the three staggered conformations at the ω torsion angle (*gt*, *gg*, and *tg*) were in good agreement with those determined from a three-state analysis of the homonuclear coupling constants as shown in Table 7.2. For the disaccharides with an equatorial hydroxyl group at C4 (**1**–**5**), essentially equal ratios of the *gt* and *gg* conformations were found, with negligible populations of *tg* both experimentally and in the

Table 7.2: Populations of the *gt*, *gg*, and *tg* conformations at the ω torsion angle in percent.

	NMR			MD		
Compound	*gt*	*gg*	*tg*	*gt*	*gg*	*tg*
1	45	49	6	45	54	1
2	60	35	5	57	42	1
3	48	46	6	48	52	0
4	35	57	8	35	65	0
5	50	43	7	57	43	0
6	55	7	38	59	15	26
7	65	7	28	70	10	20
8	57	6	37	50	20	30
9	63	4	33	65	5	30
10	73	2	25	66	6	28

simulations. A slight shift towards the *gg* conformation is found in the α-linked compounds **1** and **4**, both experimentally and from simulation.

In compounds (**6**–**10**) with an axial hydroxyl group at C4, the *gg* conformation was virtually absent based on experimental coupling constants, while the *gt* and *tg* conformations were present in a ratio of approximately 2:1. In the MD simulations, the *gg* conformation was populated to 15% and 20% in compounds **6** and **8**, compared with 10% and 5% in compounds **7** and **9**. However, from the analysis of $^3J_{\mathrm{H5,H6}R/S}$ there are no obvious differences in the population of the *gg* conformation. Instead, compounds **6** and **8** have a larger population of the *tg* conformation (38% and 37%, respectively) at the expense of the *gt* conformation.

In conclusion, there appears to be slightly lower populations of the *gt* conformation in α-D-(1→6)-linkages than in β-D-(1→6)-linkages, with an increase in the population of either the *gg* or the *tg* conformation, depending on the stereochemistry at C4. The two disaccharides with a terminal L-Fuc*p* residue show the opposite pattern; the α-L-linked compound **9** has 63% of the *gt* conformation, compared to 57% in the β-L-linked compound **8**, from experiment. From MD simulations the population of the *gt* conformation is 65% and 50% for **9** and **8**, respectively. This difference is observed as a slightly smaller value of $^3J_{\mathrm{H5,H6}R}$ for an α-D/β-L-linkage than for the corresponding β-D/α-L-linkage.

Table 7.3: Effective distances (Å) in compounds **6** and **8** from NOESY experiments and MD simulations.

	6		**8**	
Interaction	NMR	MD	NMR	MD
$\mathrm{H1}', \mathrm{H6}_{\mathrm{pro}-S}$	2.45	2.38	2.48	2.36
$\mathrm{H1}', \mathrm{H6}_{\mathrm{pro}-R}$	–[a]	2.76	–	2.78
$\mathrm{H1}', \mathrm{H6}_{\mathrm{pro}-R} + \mathrm{H4}$	–	2.74[b]	2.76	2.75
$\mathrm{H1}', \mathrm{H6}_{\mathrm{pro}-R} + \mathrm{H5}$	2.52	2.59	–	2.57
$\mathrm{H1}', \mathrm{H4}$	4.10	4.51	–	4.26
$\mathrm{H1}', \mathrm{H5}$	–	3.13	3.03	3.04
$\mathrm{H4}, \mathrm{H6}_{\mathrm{pro}-S}$	2.63	2.71	–	2.74

[a] Not determined.

[b] Combined effective distances calculated according to: $r_{a+b} = \left(r_a^{-6} + r_b^{-6}\right)^{-1/6}$.

7.3.2 The $\phi_{O5'}$ and ψ torsion angles

While the conformational distribution at the ω torsion angle is clearly important in determining the overall shape of (1→6)-linked disaccharides, also the $\phi_{O5'}$ and ψ torsion angles contribute to the three-dimensional structure.

The force field parameters related to $\phi_{O5'}$ and ψ were not changed in the new parametrization. From the MD simulations, the $\phi_{O5'}$ torsion angle was found almost exclusively ($> 96\%$) in the conformation predicted by the *exo*-anomeric effect, i.e., with $\phi_{O5'} \approx +60°$ for α-D/β-L-linkages and $\phi_{O5'} \approx -60°$ for β-D/α-L-linkages.

Experimentally, the ${}^3J_{\mathrm{C6,H1'}}$ coupling constants are approximately 0.6 Hz smaller for α-(1→6)-linkages than for β-(1→6)-linkages (Table 7.4 and Figure 7.6). This trend is not reproduced by the MD simulations, but indicates that the α-linked disaccharides have values of $\phi_{O5'}$ closer to idealized staggered values (±60°) than the β-linked compounds do (cf. Figure 1.7). Alternatively, the β-linked disaccharides have larger populations of the anti-ϕ conformation. In the MD simulation, only the β-linked compounds **2** (2.3%), **3** (3.8%), and **5** (1.4%) have more than 1% of the anti-ϕ conformation (Table 4 in Paper VI).

The values for ${}^3J_{\mathrm{C1',H6}R/S}$ indicate that the $\psi = 180°$ (*antiperiplanar*) conformation is not alone. In this conformation both coupling constants are close to 1.7 Hz, which they are not (Table 7.4). The larger magnitudes in β-linked disaccharides indicate larger populations of non-*antiperiplanar* conformations for this type of linkage than for α-linked disaccharides.

Table 7.4: Coupling constants in Hz related to the $\phi_{O5'}$ and ψ torsion angles as determined using J-HMBC experiments and from MD simulations.

Compound	$^{3}J_{C6,H1'}$ NMR	$^{3}J_{C6,H1'}$ MD	$^{3}J_{C1',H6R}$ NMR	$^{3}J_{C1',H6R}$ MD	$^{3}J_{C1',H6S}$ NMR	$^{3}J_{C1',H6S}$ MD
1	3.5	3.2	2.8	2.7	2.5	2.1
2	4.1[a]	3.3	–[b]	2.7	–	1.9
3[c]	4.3	3.4	3.2	2.1	2.8	2.2
4	3.6	3.3	2.6	2.5	2.0	1.7
5	4.2	3.4	3.5	2.5	2.7	2.0
6	3.8	3.3	2.7	2.6	2.7	1.9
7	4.3	3.3	–	2.3	2.7	2.3
8	4.5	3.3	3.2	2.6	3.8	2.4
9	–	3.3	2.8	1.9	3.2	2.5
10	n.a.[d]		2.5	2.6	1.6	1.7

[a] Olsson et al.[110]

[b] Not determined.

[c] From total line-shape analysis the values were $^{3}J_{C6,H1'}$: 3.9 Hz, $^{3}J_{C1',H6R}$: 3.1 Hz, and $^{3}J_{C1',H6S}$: 2.7 Hz.

[d] Not applicable.

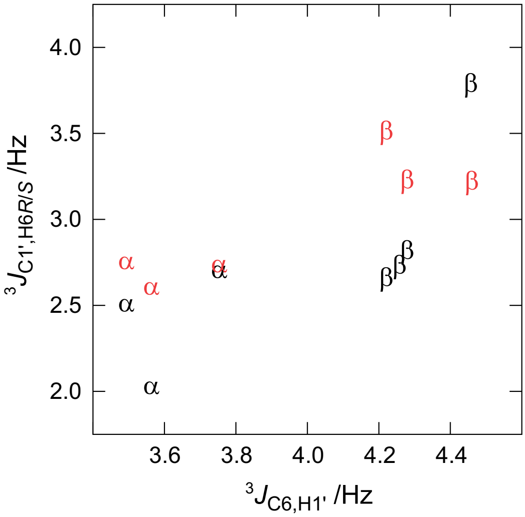

Figure 7.6: Correlation between experimental coupling constants related to $\phi_{O5'}$ and ψ for α/β-(1→6) linkages. Red and black correspond to $^{3}J_{C1',H6R}$ and $^{3}J_{C1',H6S}$, respectively.

In the MD simulations, the populations of the two *clinal* ($\psi = \pm 90°$) conformations range from 19% in compound **8** to 7% in compound **3**. The calculated values for $^3J_{\mathrm{C1'},\mathrm{H6}R/S}$ are generally slightly lower than the experimental values as seen in Table 7.4, which indicates too low populations of the *clinal* conformations at this torsion angle. Moreover, the larger values for β-linkages are not reproduced.

Table 7.5: Selected effective distances in compounds **6** and **8** in different conformations from MD simulation. Values in boldface are shorter than the experimentally determined distances.

	$r_{\mathrm{H1'},\mathrm{H4}}$ (**6**) /Å			$r_{\mathrm{H1'},\mathrm{H5}}$ (**8**) /Å		
ω	ψ : −90°	180°	+90°	−90°	180°	+90°
gt	4.97	4.88	4.16	3.69	3.99	**2.23**
gg	–[a]	5.01	4.66	4.58	4.54	3.82
tg	**3.90**	4.12	**2.30**	**2.78**	4.39	3.75

[a] Not populated in the MD simulation.

Effective distances from NOESY experiments performed on two of the compounds support populations of non-*antiperiplanar* conformations for the ψ torsion angle; the H1'-H4 distance in compound **6** is 4.1 Å, and the H1'-H5 distance in **8** is 3.0 Å. The effective distances for the different conformations of ψ and ω are shown in Table 7.5. Clearly, neither of these two distances can be achieved by the *antiperiplanar* conformations alone. For compound **6**, the H1'-H4 distance is shorter than the experimental distance only in the two *clinal*/*tg* conformations (Table 7.5). The observed distance can be explained by the $\psi = +90°/tg$ conformation having a population smaller than 3%.

For compound **8**, there is almost quantitative agreement between experiment and simulation for the H1'-H5 distance, indicating that the populations of the $\psi = +90°/gt$ and $\psi = -90°/tg$ conformations are adequately sampled. Based on the short distance in the $\psi = +90°/gt$ conformation, the population of this state cannot exceed 15%. This is close to the population (13%) in the simulation.

The magnitudes of $^2J_{\mathrm{H6}R,\mathrm{H6}S}$ are consistently too small in the MD simulations. This could be due to underestimation of the populations of *clinal* conformations at the ψ torsion angle. However, the Karplus equation[37] used was parametrized for non-substituted compounds bearing a hydroxyl group at C6 and might require adjustment before being applicable to (1→6)-linked compounds.

7.4 Conclusions

NMR parameters related to the conformational distribution at the torsion angles associated with the (1→6)-linkage in various di- and trisaccharides have been measured. The original CHARMM36 force field was shown to overestimate the relative stability of the *gg* conformation at the ω torsion angle, as determined by comparison with experimentally determined coupling constants. By using more realistic model compounds the parametrization for (1→6)-linkages in the CHARMM36 force field was improved and shown to produce conformational ensembles in better agreement with experiment.

A slight shift from population of the *gt* conformation to the *gg* and *tg* conformations was observed for α-D/β-L-linked compounds when compared to compounds with a β-D/α-L linkage. This trend was observed in the MD simulations as well as in populations derived from $^3J_{\mathrm{H5,H6}R/S}$. In this study, there is only one pair of compounds (viz. **8** and **9**) that differs only in linkage stereochemistry. However, the trend is consistent with a previous study of β-D/α-D pairs of (1→6)-linked disaccharides, where the population of the *gt* conformer was larger in the β-D-linked compounds.[123]

The values for the $^3J_{\mathrm{H1',C6}}$ coupling constant were found to be larger for β-linked compounds than for α-linked compounds, indicating that deviations from the idealized staggered *exo*-anomeric conformation at the ϕ torsion angle are larger in the β-linked compounds.

On the basis of $^3J_{\mathrm{C1',H6}R/S}$ coupling constants, the present force field is likely underestimating the populations of the *clinal* conformations ($\psi \approx \pm 90°$). Effective distances were determined from NOESY experiments in compounds **6** and **8** from H1' to H4 and H5, respectively. These distances confirm that the *clinal* conformations are present to some extent.

The improved parametrization of the CHARMM36 force field allows more realistic simulations of (1→6)-linked oligosaccharides and will hopefully lead to an improved understanding of the factors affecting their conformational preferences as well as their physical and biological properties.

This collection of experimental parameters for (1→6)-linked di- and trisaccharides obtained under similar conditions is also envisioned to be useful in further force field developments.

8. Conclusion and Outlook

Various contributions to the field of conformational studies of carbohydrates have been presented. This work represents different parts in the iterative process in which experimental data is collected, interpreted with the aid of molecular simulations, and the resulting insight used to guide the improvement of force fields.

The J-HMBC experiment was shown to give rise to complicated peak shapes for carbons adjacent to ^{13}C labeling due to homonuclear carbon-carbon couplings. Two pulse program modifications were devised, allowing the acquisition of spectra similar to those obtained for samples with a natural abundance of ^{13}C. The number of coupling constants that can be determined for a site-specifically labeled molecule has thus been increased. It would be interesting to evaluate their performance for compounds with random ^{13}C labeling.

The extent and nature of intermolecular hydrogen bonding in sucrose was investigated by MD simulations at different concentrations. An intermolcular hydrogen bond, $O3g$–$H\cdots O4f$, was detected experimentally and shown to occur frequently in the MD simulations. The highly specific intermolecular hydrogen bonding deduced by NMR spectroscopy is in contrast to the rather indiscriminate pattern in the MD simulations. Further studies are warranted to resolve the source of this apparent discrepancy.

In Chapter 4, a trisaccharide fragment of the Le^{a}Le^{x} hexasaccharide was found to be flexible at its *β*-D-Glc*p*NAc-(1→3)-*β*-D-Gal*p* linkage in MD simulations using three different force fields, with two conformations having positive and negative values for the ψ_3 torsion angle. The two most recent force fields gave the most accurate representations of the conformational preferences in this trisaccharide as deduced by comparison with data from NMR spectroscopy. Available experimental parameters do not allow the distinction to be made between a single conformation or two conformations at the *β*-D-Glc*p*NAc-(1→3)-*β*-D-Gal*p* linkage and thus it would be beneficial to measure additional coupling constants in this compound.

Correlations between the conformation at the glycosidic linkage and the conformation of nearby *N*-acetyl substituents were observed in MD simulations of the two oligosaccharides described in Chapter 5. The causal relationships were determined to be due to combinations of steric effects and hydrogen bonding. For LNF-1, the *N*-acetyl substituent was shown to exhibit slower dynamics than any of the glycosidic bonds. This finding highlights the importance of monitoring other degrees of freedom in addition to the ones primarily under investigation.

The disaccharide β-L-Fuc*p*-(1→6)-α-D-Glc*p*-OMe was shown in Chapter 6 to tumble in an axially symmetric fashion, leading to different ^{13}C T_1 relaxation times for carbons with similar internal dynamics. Additionally, it was found that at least two conformations at both of the ω and ψ torsion angles are required to explain the experimental data. Notably, a conformation with $\psi \approx 85^\circ$ was found to be present to approximately 30%.

NMR parameters sensitive to the conformational distributions at the (1→6)-linkages in ten di- and trisaccharides were measured in Chapter 7. These were used to guide the refinement of parameters for the ω torsion angle in the CHARMM36 force field, leading to a more accurate representation of compounds containing (1→6)-linkages. The populations of the *clinal* conformations with $\psi \approx \pm 90^\circ$ are likely underestimated in both of the PARM22/SU01 and CHARMM36 force fields, according to the $^{3}J_{\mathrm{C1'},\mathrm{H6}R/S}$ coupling constants. Further investigations should lead to the unraveling of the influences of various factors on the conformational distribution at (1→6)-linkages.

The insight into conformational preferences of short oligosaccharides can be used to guide further refinement of force fields for carbohydrates, as was done in Chapter 7. As force fields are improved, predictions and determinations of conformational preferences can be made with higher confidence. Additionally, knowledge of accessible conformations in small fragments can be useful in the determination of conformational preferences in larger molecules in which the same fragments occur.

The ability to determine and predict conformations in oligo- and polysaccharides in an accurate way will likely play a major role in elucidating the complicated relationship between the structures of carbohydrates and their biological and physical properties.

Acknowledgments

I am grateful to *Göran Widmalm* for guidance and support, and for being available for long discussions in your office.

Jan-Erling Bäckvall for showing interest in my work and for valuable comments on this thesis.

My collaborators on the various projects; *Ole W. Sørensen*, *Daron I. Freedberg*, *Marcos D. Battistel*, *Mona Zaccheus*, members in the group of *France-Isabelle Auzanneau*, *K. Hanna M. Jonsson*, *Elin Säwén*, and *Alexander D. MacKerell, Jr.* and members of his group.

John Brady, *Mo Chen*, and *Teppei Tamaki* for great times during my visit to Cornell University.

Christoffer Hamark, *Jerk Rönnols*, *Olof Engström*, and *Teresa* for reading and improving this thesis. *Teresa* for reading the title.

Past and present members of the GW group; *Anja*, *Jens L.*, *Hanna*, *Elin*, *Magnus*, *Mona*, *Jerk*, *Carolina*, *Christoffer*, *Olle*, *Thibault*, *Hani*, and *Jonas* for friendships, BLOs, etc.

Jerk, *Jens F.* and *Clinton* for onsen, ramen and äggbrunor in the land of the rising sun, *Christoffer* and *Jerk* for the jazz in the land of the free, and *Thibault*, *Carolina* and *Jerk* for tapas.

Nanna, *Jerk*, and *Christoffer* for musical communion. *Johannes* for fikas and NMR chats. *Anders* and *Staffan* for vetenskapsöl.

Everyone at the department for contributing to a nice and friendly environment.

Torbjörn for help with and nice discussions about the spectrometers. *Helena Kovacs* for help with pulse programming.

The technical and administrative personnel, for fixing, helping, and for reminding me to fill out forms.

The *PDC Center for High Performance Computing* and the *National Supercomputer Centre in Linköping* for providing computing resources and technical support.

The *Knut & Alice Wallenberg foundation*, *Ångpanneföreningens forskningsstiftelse*, *Svenska Kemistsamfundet*, *SMASH*, and *Stockholms Universitet* for financially supporting my travels to conferences around the world and my stay in Ithaca.

My family for encouragement, care, and scientific discussions throughout the years.

Teresa for food, love, and kinetic data.

Bibliography

[1] Varki, A., Cummings, R. D., Esko, J. D., Freeze, H. H., Stanley, P., Bertozzi, C. R., Hart, G. W., Etzler, M. E., Eds. *Essentials of Glycobiology;* Cold Spring Harbor Laboratory Press: New York, 2nd ed., 2009.

[2] Widmalm, G. *Carbohydr. Res.* **2013**, *378*, 123–132.

[3] Holme, T.; Rahman, M.; Jansson, P.-E.; Widmalm, G. *Eur. J. Biochem.* **1999**, *265*, 524–529.

[4] Almond, A.; Brass, A.; Sheehan, J. K. *J. Phys. Chem. B* **2000**, *104*, 5634–5640.

[5] Lycknert, K.; Widmalm, G. *Biomacromolecules* **2004**, *5*, 1015–1020.

[6] Juaristi, E.; Cuevas, G. *Tetrahedron* **1992**, *48*, 5019–5087.

[7] Sattelle, B. M.; Almond, A. *Phys. Chem. Chem. Phys.* **2012**, *14*, 5843–5848.

[8] IUPAC-IUB Joint Commission on Biochemical Nomenclature. *Eur. J. Biochem.* **1983**, *131*, 5–7.

[9] Praly, J.-P.; Lemieux, R. U. *Can. J. Chem.* **1987**, *65*, 213–223.

[10] Wolfe, S. *Acc. Chem. Res.* **1972**, *5*, 102–111.

[11] Bock, K.; Duus, J. Ø. *J. Carbohydr. Chem.* **1994**, *13*, 513–543.

[12] Hassel, O.; Ottar, B. *Acta Chem. Scand.* **1947**, *1*, 929–943.

[13] Jeffrey, G. A. *Acta Crystallogr. Sect. B Struct. Sci.* **1990**, *46*, 89–103.

[14] Brady, J. W.; Schmidt, R. K. *J. Phys. Chem.* **1993**, *97*, 958–966.

[15] Kirschner, K. N.; Woods, R. J. *Proc. Natl. Acad. Sci. U. S. A.* **2001**, *98*, 10541–10545.

[16] Barnett, C. B.; Naidoo, K. J. *J. Phys. Chem. B* **2008**, *112*, 15450–15459.

[17] O'Dell, W. B.; Baker, D. C.; McLain, S. E. *PLoS One* **2012**, *7*, e45311.

[18] Perić-Hassler, L.; Hansen, H. S.; Baron, R.; Hünenberger, P. H. *Carbohydr. Res.* **2010**, *345*, 1781–1801.

[19] Wang, D.; Ámundadóttir, M. L.; van Gunsteren, W. F.; Hünenberger, P. H. *Eur. Biophys. J.* **2013**, *42*, 521–537.

[20] Chu, S. S. C.; Jeffrey, G. A. *Acta Crystallogr. Sect. B* **1968**, *24*, 830–838.

[21] Liu, Q.; Brady, J. W. *J. Am. Chem. Soc.* **1996**, *118*, 12276–12286.

[22] Engelsen, S. B.; Monteiro, C.; Hervé de Penhoat, C.; Pérez, S. *Biophys. Chem.* **2001**, *93*, 103–127.

[23] Ramadugu, S. K.; Chung, Y.-H.; Xia, J.; Margulis, C. J. *J. Phys. Chem. B* **2009**, *113*, 11003–11015.

[24] Duus, J. Ø.; Gotfredsen, C. H.; Bock, K. *Chem. Rev.* **2000**, *100*, 4589–4614.

[25] Wormald, M. R.; Petrescu, A. J.; Pao, Y.-L.; Glithero, A.; Elliott, T.; Dwek, R. A. *Chem. Rev.* **2002**, *102*, 371–386.

[26] Kochetkov, N. K.; Chizhov, O. S.; Shashkov, A. S. *Carbohydr. Res.* **1984**, *133*, 173–185.

[27] Hori, H.; Nishida, Y.; Ohrui, H.; Meguro, H.; Uzawa, J. *Tetrahedron Lett.* **1988**, *29*, 4457–4460.

[28] De Bruyn, A. *J. Carbohydr. Chem.* **1991**, *10*, 159–180.

[29] Bock, K.; Brignole, A.; Sigurskjold, B. W. *J. Chem. Soc. Perkin Trans. 2* **1986**, 1711–1713.

[30] Zierke, M.; Smieško, M.; Rabbani, S.; Aeschbacher, T.; Cutting, B.; Allain, F. H.-T.; Schubert, M.; Ernst, B. *J. Am. Chem. Soc.* **2013**, *135*, 13464–13472.

[31] Swalina, C. W.; Zauhar, R. J.; DeGrazia, M. J.; Moyna, G. *J. Biomol. NMR* **2001**, *21*, 49–61.

[32] O'Brien, E. P.; Moyna, G. *Carbohydr. Res.* **2004**, *339*, 87–96.

[33] Prestegard, J. H.; Bougault, C. M.; Kishore, A. I. *Chem. Rev.* **2004**, *104*, 3519–3540.

[34] Bryant, R. G. *J. Chem. Educ.* **1983**, *60*, 933–935.

[35] Coxon, B. *Adv. Carbohydr. Chem. Biochem.* **2009**, *62*, 17–82.

[36] Stenutz, R.; Carmichael, I.; Widmalm, G.; Serianni, A. S. *J. Org. Chem.* **2002**, *67*, 949–958.

[37] Thibaudeau, C.; Stenutz, R.; Hertz, B.; Klepach, T.; Zhao, S.; Wu, Q.; Carmichael, I.; Serianni, A. S. *J. Am. Chem. Soc.* **2004**, *126*, 15668–15685.

[38] Säwén, E.; Massad, T.; Landersjö, C.; Damberg, P.; Widmalm, G. *Org. Biomol. Chem.* **2010**, *8*, 3684–3695.

[39] Laatikainen, R.; Niemitz, M.; Weber, U.; Sundelin, J.; Hassinen, T.; Vepsäläinen, J. *J. Magn. Reson. Ser. A* **1996**, *120*, 1–10.

[40] Nath, N.; Lokesh.; Suryaprakash, N. *ChemPhysChem* **2012**, *13*, 645–660.

[41] Parella, T.; Espinosa, J. F. *Prog. Nucl. Magn. Reson. Spectrosc.* **2013**, *73*, 17–55.

[42] Meissner, A.; Sørensen, O. W. *Magn. Reson. Chem.* **2001**, *39*, 49–52.

[43] Koźmiski, W.; Nanz, D. *J. Magn. Reson.* **1997**, *124*, 383–392.

[44] Ottiger, M.; Bax, A. *J. Am. Chem. Soc.* **1998**, *120*, 12334–12341.

[45] Doddrell, D. *J. Chem. Phys.* **1972**, *56*, 3683–3689.

[46] Lipari, G.; Szabo, A. *J. Am. Chem. Soc.* **1982**, *104*, 4546–4559.

[47] Stott, K.; Keeler, J.; Van, Q. N.; Shaka, A. J. *J. Magn. Reson.* **1997**, *125*, 302–324.

[48] Kjellberg, A.; Widmalm, G. *Biopolymers* **1999**, *50*, 391–399.

[49] Neuhaus, D.; Williamson, M. P. *The Nuclear Overhauser Effect in Structural and Conformational Analysis*, Methods in Stereochemical Analysis; Wiley-VCH: New York, 2nd ed., 2000.

[50] Wüthrich, K. *Science.* **1989**, *243*, 45–50.

[51] Davis, D. G. *J. Am. Chem. Soc.* **1987**, *109*, 3471–3472.

[52] Karplus, M.; McCammon, J. A. *Nat. Struct. Biol.* **2002**, *9*, 646–652.

[53] Foley, B. L.; Tessier, M. B.; Woods, R. J. *WIREs Comput. Mol. Sci.* **2012**, *2*, 652–697.

[54] Eklund, R.; Widmalm, G. *Carbohydr. Res.* **2003**, *338*, 393–398.

[55] Guvench, O.; Greene, S. N.; Kamath, G.; Brady, J. W.; Venable, R. M.; Pastor, R. W.; MacKerell, Jr., A. D. *J. Comput. Chem.* **2008**, *29*, 2543–2564.

[56] Guvench, O.; Mallajosyula, S. S.; Raman, E. P.; Hatcher, E.; Vanommeslaeghe, K.; Foster, T. J.; Jamison, F. W.; MacKerell, Jr., A. D. *J. Chem. Theory Comput.* **2011**, *7*, 3162–3180.

[57] Kirschner, K. N.; Yongye, A. B.; Tschampel, S. M.; González-Outeiriño, J.; Daniels, C. R.; Foley, B. L.; Woods, R. J. *J. Comput. Chem.* **2008**, *29*, 622–655.

[58] Woods, R. J.; Tessier, M. B. *Curr. Opin. Struct. Biol.* **2010**, *20*, 575–583.

[59] Jardetzky, O. *Biochim. Biophys. Acta* **1980**, *621*, 227–232.

[60] Catalano, D.; Di Bari, L.; Veracini, C. A.; Shilstone, G. N.; Zannoni, C. *J. Chem. Phys.* **1991**, *94*, 3928–3935.

[61] Dzakula, Z.; Westler, W. M.; Edison, A. S.; Markley, J. L. *J. Am. Chem. Soc.* **1992**, *114*, 6195–6199.

[62] Blundell, C. D.; Packer, M. J.; Almond, A. *Bioorg. Med. Chem.* **2013**, *21*, 4976–4987.

[63] Säwén, E.; Stevensson, B.; Östervall, J.; Maliniak, A.; Widmalm, G. *J. Phys. Chem. B* **2011**, *115*, 7109–7121.

[64] Cumming, D. A.; Carver, J. P. *Biochemistry* **1987**, *26*, 6664–6676.

[65] Thomas, W. *Prog. Nucl. Magn. Reson. Spectrosc.* **1997**, *30*, 183–207.

[66] Rundlöf, T.; Kjellberg, A.; Damberg, C.; Nishida, T.; Widmalm, G. *Magn. Reson. Chem.* **1998**, *36*, 839–847.

[67] Saurí, J.; Parella, T. *Magn. Reson. Chem.* **2013**, *51*, 397–402.

[68] Podlasek, C. A.; Wu, J.; Stripe, W. A.; Bondo, P. B.; Serianni, A. S. *J. Am. Chem. Soc.* **1995**, *117*, 8635–8644.

[69] Jonsson, K. H. M.; Säwén, E.; Widmalm, G. *Org. Biomol. Chem.* **2012**, *10*, 2453–2463.

[70] Bax, A.; Freeman, R. *J. Magn. Reson.* **1981**, *44*, 542–561.

[71] Brüschweiler, R.; Griesinger, C.; Sørensen, O. W.; Ernst, R. R. *J. Magn. Reson.* **1988**, *78*, 178–185.

[72] Marino, J. P.; Diener, J. L.; Moore, P. B.; Griesinger, C. *J. Am. Chem. Soc.* **1997**, *119*, 7361–7366.

[73] Jonsson, K. H. M.; Pendrill, R.; Widmalm, G. *Magn. Reson. Chem.* **2011**, *49*, 117–124.

[74] Olsson, U.; Serianni, A. S.; Stenutz, R. *J. Phys. Chem. B* **2008**, *112*, 4447–4453.

[75] Brown, G. M.; Levy, H. A. *Acta Crystallogr. Sect. B* **1973**, *29*, 790–797.

[76] Bock, K.; Lemieux, R. U. *Carbohydr. Res.* **1982**, *100*, 63–74.

[77] McCain, D. C.; Markley, J. L. *Carbohydr. Res.* **1986**, *152*, 73–80.

[78] Mulloy, B.; Frenkiel, T. A.; Davies, D. B. *Carbohydr. Res.* **1988**, *184*, 39–46.

[79] Tran, V. H.; Brady, J. W. *Biopolymers* **1990**, *29*, 961–976.

[80] Tran, V. H.; Brady, J. W. *Biopolymers* **1990**, *29*, 977–997.

[81] Hervé du Penhoat, C.; Imberty, A.; Roques, N.; Michon, V.; Mentech, J.; Descotes, G.; Pérez, S. *J. Am. Chem. Soc.* **1991**, *113*, 3720–3727.

[82] Poppe, L.; van Halbeek, H. *J. Am. Chem. Soc.* **1992**, *114*, 1092–1094.

[83] Xia, J.; Case, D. A. *Biopolymers* **2012**, *97*, 276–288.

[84] Adams, B.; Lerner, L. *J. Am. Chem. Soc.* **1992**, *114*, 4827–4829.

[85] Sheng, S.; van Halbeek, H. *Biochem. Biophys. Res. Commun.* **1995**, *215*, 504–510.

[86] Battistel, M. D.; Shangold, M.; Trinh, L.; Shiloach, J.; Freedberg, D. I. *J. Am. Chem. Soc.* **2012**, *134*, 10717–10720.

[87] Bax, A.; Ikura, M.; Kay, L. E.; Torchia, D. A.; Tschudin, R. *J. Magn. Reson.* **1990**, *86*, 304–318.

[88] Cremer, D.; Pople, J. A. *J. Am. Chem. Soc.* **1975**, *97*, 1354–1358.

[89] Levery, S. B. Cancer-Associated and Related Glycosphingolipid Antigens, In *Carbohydrate-Based Vaccines Immunotherapies*; Gou, Z., Boons, G.-J., Eds.; Wiley: Hoboken, NJ, USA, 2009; chapter 8, pages 245–280.

[90] Wilson, R. M.; Danishefsky, S. J. *J. Am. Chem. Soc.* **2013**, *135*, 14462–14472.

[91] Battifora, H.; Sorensen, H. R.; Mehta, P.; Ahn, C.; Niland, J.; Hage, E.; Pettijohn, D. E.; Olsson, L. *Cancer* **1992**, *70*, 1867–1872.

[92] Lemieux, R. U.; Baker, D. A.; Weinstein, W. M.; Switzer, C. M. *Biochemistry* **1981**, *20*, 199–205.

[93] Jackson, T. A.; Robertson, V.; Imberty, A.; Auzanneau, F.-I. *Bioorg. Med. Chem.* **2009**, *17*, 1514–1526.

[94] Martin-Pastor, M.; Bush, C. *Carbohydr. Res.* **1999**, *323*, 147–155.

[95] Kotsyubynskyy, D.; Zerbetto, M.; Soltesova, M.; Engström, O.; Pendrill, R.; Kowalewski, J.; Widmalm, G.; Polimeno, A. *J. Phys. Chem. B* **2012**, *116*, 14541–14555.

[96] Landersjö, C.; Jansson, J. L. M.; Maliniak, A.; Widmalm, G. *J. Phys. Chem. B* **2005**, *109*, 17320–17326.

[97] Lemieux, R. U.; Bock, K.; Delbaere, L. T. J.; Koto, S.; Rao, V. S. *Can. J. Chem.* **1980**, *58*, 631–653.

[98] Cagas, P.; Bush, C. A. *Biopolymers* **1990**, *30*, 1123–1138.

[99] Azurmendi, H. F.; Martin-Pastor, M.; Bush, C. A. *Biopolymers* **2002**, *63*, 89–98.

[100] Bekiroglu, S.; Kenne, L.; Sandström, C. *Carbohydr. Res.* **2004**, *339*, 2465–2468.

[101] Pastor, R. Techniques and Applications of Langevin Dynamics Simulations, In *The Molecular Dynynamics of Liquid Crystals*; Luckhurst, G. R., Veracini, C. A., Eds.; Kluwer Academic Publishers, 1994; chapter 5, pages 85–138.

[102] Almond, A.; Brass, A.; Sheehan, J. K. *Glycobiology* **1998**, *8*, 973–980.

[103] Donati, A.; Magnani, A.; Bonechi, C.; Barbucci, R.; Rossi, C. *Biopolymers* **2001**, *59*, 434–445.

[104] Hu, X.; Zhang, W.; Carmichael, I.; Serianni, A. S. *J. Am. Chem. Soc.* **2010**, *132*, 4641–4652.

[105] Almond, A.; Petersen, B. O.; Duus, J. Ø. *Biochemistry* **2004**, *43*, 5853–5863.

[106] Cagas, P.; Kaluarachchi, K.; Bush, C. A. *J. Am. Chem. Soc.* **1991**, *113*, 6815–6822.

[107] Bock, K.; Duus, J. Ø.; Hindsgaul, O.; Lindh, I. *Carbohydr. Res.* **1992**, *228*, 1–20.

[108] Lycknert, K.; Edblad, M.; Imberty, A.; Widmalm, G. *Biochemistry* **2004**, *43*, 9647–9654.

[109] Corzana, F.; Motawia, M. S.; Hervé du Penhoat, C.; Pérez, S.; Tschampel, S. M.; Woods, R. J.; Engelsen, S. B. *J. Comput. Chem.* **2004**, *25*, 573–586.

[110] Olsson, U.; Säwén, E.; Stenutz, R.; Widmalm, G. *Chemistry.* **2009**, *15*, 8886–8894.

[111] Hu, H.; Bradley, S. A.; Krishnamurthy, K. *J. Magn. Reson.* **2004**, *171*, 201–206.

[112] Marchessault, R. H.; Perez, S. *Biopolymers* **1979**, *18*, 2369–2374.

[113] Svishchev, I. M.; Kusalik, P. G. *J. Chem. Phys.* **1993**, *99*, 3049–3058.

[114] Bloomfield, V. A. Survey of Biomolecular Hydrodynamics, In *On-Line Biophysics Textbook: Separations and Hydrodynamics*; Schuster, T. M., Ed.; 2000; chapter 1, pages 1–16.

[115] Berry, J. M.; Hall, L. D.; Wong, K. F. *Carbohydr. Res.* **1977**, *56*, C16–C20.

[116] Hayes, M. L.; Serianni, A. S.; Barker, R. *Carbohydr. Res.* **1982**, *100*, 87–101.

[117] Farmer, II, B. T.; Macura, S.; Brown, L. R. *J. Magn. Reson.* **1988**, *80*, 1–22.

[118] Rundlöf, T.; Venable, R. M.; Pastor, R. W.; Kowalewski, J.; Widmalm, G. *J. Am. Chem. Soc.* **1999**, *121*, 11847–11854.

[119] Guvench, O.; Hatcher, E. R.; Venable, R. M.; Pastor, R. W.; MacKerell, Jr., A. D. *J. Chem. Theory Comput.* **2009**, *5*, 2353–2370.

[120] Eklund, R.; Lycknert, K.; Söderman, P.; Widmalm, G. *J. Phys. Chem. B* **2005**, *109*, 19936–19945.

[121] Zaccheus, M.; Pendrill, R.; Jackson, T. A.; Wang, A.; Auzanneau, F.-I.; Widmalm, G. *European J. Org. Chem.* **2012**, 4705–4715.

[122] Faraldo-Gómez, J. D.; Roux, B. *J. Comput. Chem.* **2007**, *28*, 1634–1647.

[123] Jansson, P.-E.; Kenne, L.; Kolare, I. *Carbohydr. Res.* **1994**, *257*, 163–174.